

**ERT**

Document P-1456  
Type 3 Report  
October 1976

Prepared for  
National Aeronautics and Space Administration  
Goddard Space Flight Center  
Greenbelt, Maryland

# Fabrication and testing of an airborne ice particle counter

Prepared by  
Paul L. Keabian

**Page  
Intentionally  
Left Blank**

1. Report No.		2. Government Accession No.		3. Recipient's Catalog No.	
4. Title and Subtitle Fabrication and Testing of an Airborne Ice Particle Counter				5. Report Date October 1976	
				6. Performing Organization Code	
7. Author(s) Paul L. Keabian				8. Performing Organization Report No. P1456	
9. Performing Organization Name and Address Environmental Research & Technology, Inc. 696 Virginia Road, Concord, MA.				10. Work Unit No.	
				11. Contract or Grant No. NAS 5-20911	
12. Sponsoring Agency Name and Address National Aeronautics and Space Administration Goddard Space Flight Center Greenbelt, Maryland 20771				13. Type of Report and Period Covered Final Report (Type III) 31 Dec. 1974 - 31 Jul. 1976	
				14. Sponsoring Agency Code	
15. Supplementary Notes					
16. Abstract  <p>The purpose of this project was to build an optical ice particle counter as a companion instrument to the GSFC Laser Nephelometer. By counting ice particles and total cloud particles (both ice and liquid water), these two instruments may be used to study the balance between ice and water in clouds.</p> <p>The design of this ice particle counter was adopted from a sensor developed at the University of Washington, [1], [2], with particular attention focused on its mechanical design, so that it will be suitable for use on a relatively high-speed aircraft such as the NASA CV-990.</p>					
17. Key Words (Suggested by Author(s)) Cloud Physics Ice Crystals Aircraft Instrumentation				18. Distribution Statement Unclassified-Unlimited	
19. Security Classif. (of this report) Unclassified		20. Security Classif. (of this page) Unclassified		21. No. of Pages 70	22. Price*

**Page  
Intentionally  
Left Blank**

100

10

## ACKNOWLEDGEMENTS

Special thanks are due to the University of Washington researchers, Dr. F. M. Turner, Professor L. Radke and Professor P. Hobbs, for the original sensor design and their invaluable assistance during the fabrication and testing of the ice particle counter described in this report.

We also wish to thank Mr. Chyau Shen, of the Naval Air Propulsion Test Center, Trenton, N.J., for his help in the initial testing of the ice particle counter at that facility.

The detailed mechanical design of this instrument was by Mr. G. Roberts of Amdek Corporation, Sudbury, Mass.

**Page  
Intentionally  
Left Blank**

## TABLE OF CONTENTS

	Page
1. INTRODUCTION	1
2. THEORY OF OPERATION	3
2.1 Rejection of Water Drops	3
2.2 Detection of Ice Crystals	6
2.3 Case 1: Thin Plate	7
2.4 Case 2: Small, Short Column	12
2.5 Case 3: Large or Very Birefringent Column with $t \sim d$	12
2.6 Case 4: Column with $t \gg d$ and Smooth Facets	12
2.7 Case 5: Column with $t \gg d$ and Rough Facets	15
2.8 Case 6: Internal Reflecting Column with $t \gg d$	16
2.9 Case 7: Thin, Internally Reflecting Plate	16
3. MECHANICAL DESIGN	19
4. ELECTRONICS AND SIGNAL PROCESSING	27
5. PRELIMINARY TESTING	37
6. CALIBRATION AT UNIVERSITY OF WASHINGTON	43
7. CONCLUSIONS, SUMMARY AND SUGGESTIONS FOR FUTURE RESEARCH	49
8. REFERENCES	53
APPENDIX A ASSEMBLY AND DISASSEMBLY INSTRUCTIONS FOR THE ICE PARTICLE COUNTER	A-1

**Page  
Intentionally  
Left Blank**

## LIST OF ILLUSTRATIONS

Figure		Page
2-1	Basic Geometry of Ice Particle Counter Optics	4
2-2	Mask Located behind Polarizer in $x'' - y''$ Plane	5
2-3	Geometry of Case 1	8
2-4	Cross Section of the Index Ellipsoid of a Uniaxial Crystal	8
2-5	Function $1 - J_0^2(x) - J_1^2(x)$ Representing the Fraction of Total Energy Contained within Circles of Prescribed Radii in the Fraunhofer Diffraction Pattern of a Circular Aperture Points show the approximation $1 - 2/\pi x$ .	10
2-6	Graph of $f^2(\theta_e, 1.3) \sqrt{\cos\theta_e}$	13
2-7	Diffraction Pattern of Columnar Ice Particle	14
2-8	Scattering into Mask Plane from Internal Reflecting Column with $t \gg d$	17
3-1	Assembled View of Ice Particle Counter; Tools for Assembly and Disassembly	20
3-2	Ice Particle Counter - Disassembled	21
3-3	Detail of Laser	22
3-4	Detail of Phototube	23
3-5	Ice Particle Counter as Mounted to an Aircraft	24
4-1	Calibration of PMT, EMI-Gencom Type MPD/IR/DCDC S/N 5799	28
4-2	Signal Processing Circuit The operational amplifiers are CA3130AT (Mfg. RCA), the comparators are LM311 (Mfg. NS), and the NOR gates are CD4001AE (Mfg. RCA).	29
4-3	Calibration Curve of a Quasi-log Amplifier At low input currents, transresistance = $10^5 \Omega$ (V output = 0.1i input).	30
4-4	The Function $w/\sigma = 2\sqrt{2} \ln s/s_0$	34

## LIST OF ILLUSTRATIONS (Continued)

Figure		Page
5-1	Measured Distribution of Areas of a Sample of Sugar Crystals Used in Testing the Ice Particle Counter	38
5-2	Internal Reflection in a Cubic Crystal	40
	a. Single Reflection - Ray Is Deviated through a Large Angle	
	b. Two Reflections - Ray Leaves Parallel to Incident Ray	
6-1	Relative Counting Rates of the Two Ice Particles Counters as a Function of the Average Maximum Diameter of Particles Being Counted	45
	The pairs of points are the results for counting immediately before and after the replica was taken, from which the particle size distribution was measured.	
6-2a	Particle Size Distribution	46
6-2b	Pulse Height Distribution	46

## 1. INTRODUCTION

The purpose of this project was to build an optical ice particle counter as a companion instrument to the GSFC Laser Nephelometer. By counting ice particles and total cloud particles (both ice and liquid water), these two instruments may be used to study the balance between ice and water in clouds.

The design of this ice particle counter was adopted from a sensor developed at the University of Washington, [1], [2], with particular attention focused on its mechanical design, so that it will be suitable for use on a relatively high-speed aircraft such as the NASA CV-990.

**Page  
Intentionally  
Left Blank**

2

## 2. THEORY OF OPERATION

The optics of the ice particle counter have been designed to obtain optimum rejection of water drops while detecting ice crystals. This is done by observing the change in the polarization of incident light when it is scattered in a near forward direction by an ice particle, whereas a water droplet does not produce a correspondingly large change.

Figure 2-1 shows the basic geometry of the ice particle counter's optics. The source is a laser, polarized with its electric field in the  $x$  direction and transmitted in the  $-z$  direction.

### 2.1 Rejection of Water Drops

The theory of how the ice particle counter rejects the light scattered by water droplets is described in detail in [1]; what follows is only a qualitative summary.

From symmetry considerations, it can be seen that when the scatterer is a spherical, isotropic object located along the  $z$  axis, the scattered radiation striking the detector plane along the  $x''$  and  $z''$  axes must have the same polarization as the incident light. Thus, a polarizer which transmits light with its electric field along the  $y''$  axis will suppress the scattered light in the vicinity of the  $x''$  and  $z''$  axes, and an arbitrarily high degree of suppression can be obtained by limiting observations to a sufficiently narrow region around the axes.

The water droplets of interest in atmospheric studies are quite accurately spherical (within a few percent, for droplets up to several hundred microns diameter), and they are, of course, isotropic. Thus, by detecting the light scattered into the vicinity of the axes, and polarized perpendicularly to the incident light, scattering from water drops is suppressed.

Since the diffraction of light by a spherical isotropic body can be solved exactly, it is possible to calculate the best compromise between an open area in which light is detected and the degree of rejection of water drops, without the considerable difficulties involved in finding this by experiment.

This is done in [1], and the resulting mask, located behind a polarizer in the  $x''-y''$  plane, is shown in Figure 2-2.

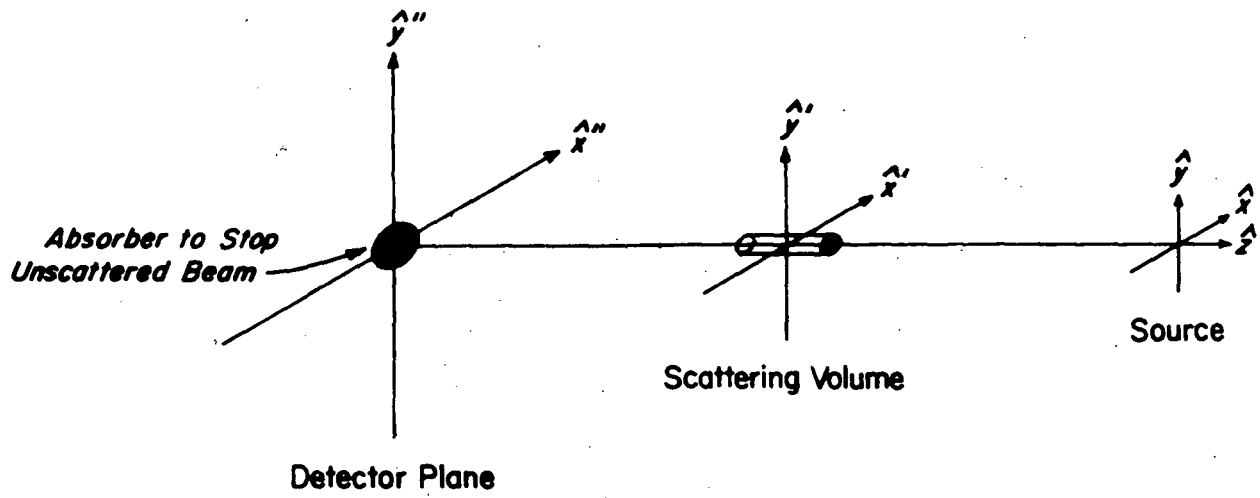


Figure 2-1 Basic Geometry of Ice Particle Counter Optics

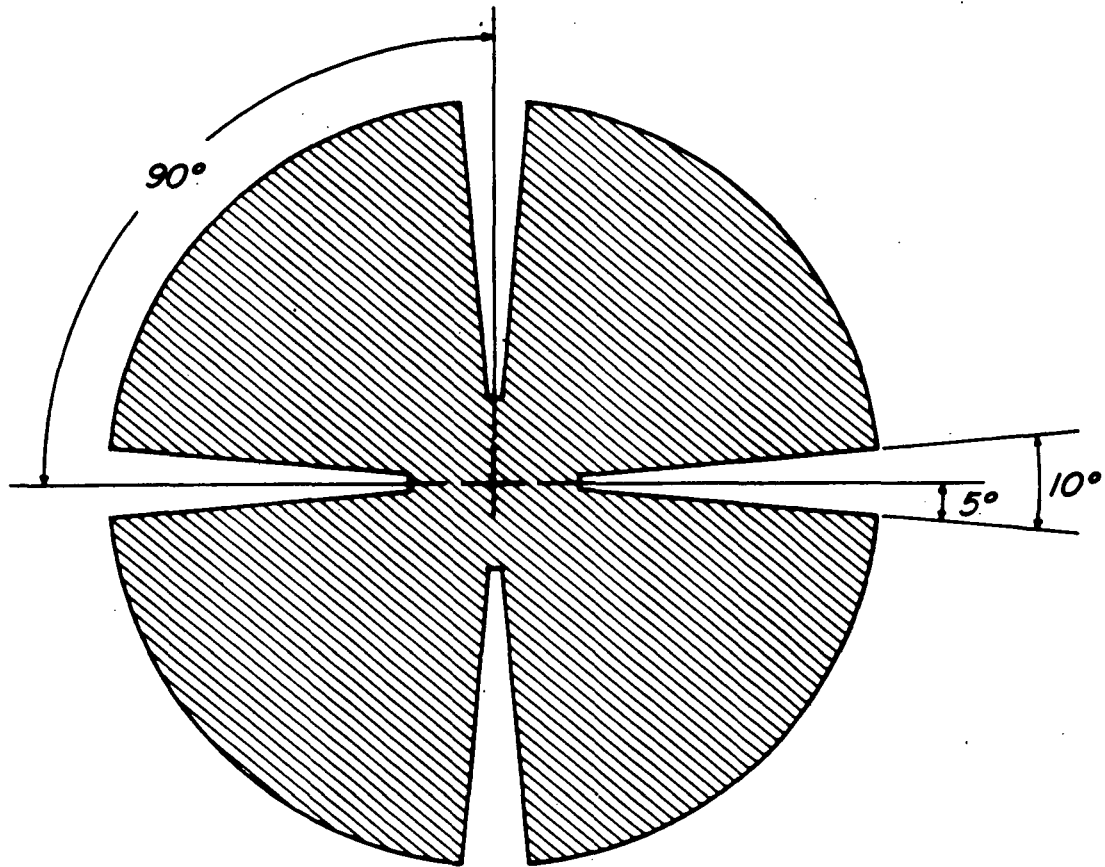


Figure 2-2 Mask Located behind Polarizer in  $x'' - y''$  Plane

## 2.2 Detection of Ice Crystals

The polarization of the light scattered from an ice crystal, into the region of the detector plane where the mask of Figure 2-2 is transmissive, is rotated from its initial state mainly because ice is birefringent, and because internal reflections can occur as it is transmitted through the crystal. Specular reflections off the external faces of the crystal can also depolarize the light to some extent, but, as shown in [1], this is a relatively minor effect.

Due to the many complex forms assumed by real ice crystals, it is not possible to compute their scattering properties exactly, as in the case of spherical water drops. The purpose of the calculations which follow is to obtain an approximate theoretical estimate of the power scattered by several forms of ice crystal, to be compared with experimental observations.

For typical ice particles observed in the calibration of the instrument of maximum dimension  $d$ ,  $20\mu < d < 200\mu$ , and for wavelength  $\lambda = 0.6328\mu$ , then  $\lambda \ll d$  and the detector is in the far field region, i.e.,  $d < \sqrt{\lambda r}$ , where  $r$  is the spacing from the scattering volume to the detector,  $\sim 2 \times 10^5\mu$  in this case. Therefore, it is reasonable to calculate the scattered radiation using Fraunhofer diffraction theory. In that approximation, as used here, the distribution of radiation in a plane immediately behind the particle and perpendicular to the direction of the incident beam, is found using geometrical optics. The only components of interest are those polarized perpendicularly to the incident polarization, and propagating in the direction of the incident light; that is, rays that have been bent by passing through a pair of non-parallel facets on the crystal are not considered. Finally, the diffracted light is represented as resulting from the diffraction of a uniform plane wave by an opaque screen that transmits only where the component has a significant amplitude, and the shape of the aperture in the screen is replaced by a simpler figure, a circle or rectangle, of the same area.

### 2.3 Case 1: Thin Plate

The geometry of this case is shown in Figure 2-3. The diameter of the plate (across the points) is  $d$  and its thickness is  $t$ . If it were oriented with the normal to its surface along  $z'$ , the direction of the incident light, then the polarization of the transmitted light would be unchanged. For a given angle of the normal with respect to the  $z'$  axis, the largest effect on the polarization occurs when the projection of the normal onto the  $x'-y'$  plane is at  $45^\circ$  to those axes. Since the purpose of these calculations is to find the largest signal to be expected from a given crystal, that is the orientation to be considered.

The refractive index of the crystal is described by its index ellipsoid, a section of which is shown in Figure 2-4. Since ice is a uniaxial crystal, the section is the same for any plane containing the optical axis ( $\hat{p}$  of Figure 2-4). As explained in [3], the two refractive indices characterizing the propagation of a wave through the crystal may be calculated geometrically from this ellipsoid. Using the fact that  $n_o \approx n_e \approx 1.3 = n$  and  $\delta = n_e - n_o = 0.0014 \ll n$ , it is easy to verify that

$$\Delta n = \delta \frac{\tan^2 \theta_i}{1 + \tan^2 \theta_i},$$

where  $\Delta n$  is the difference in refractive index for light polarized in a plane containing the optical axis and which is perpendicular to that polarization. Rewriting this in terms of the external angle of incidence,  $\theta_e$ ,

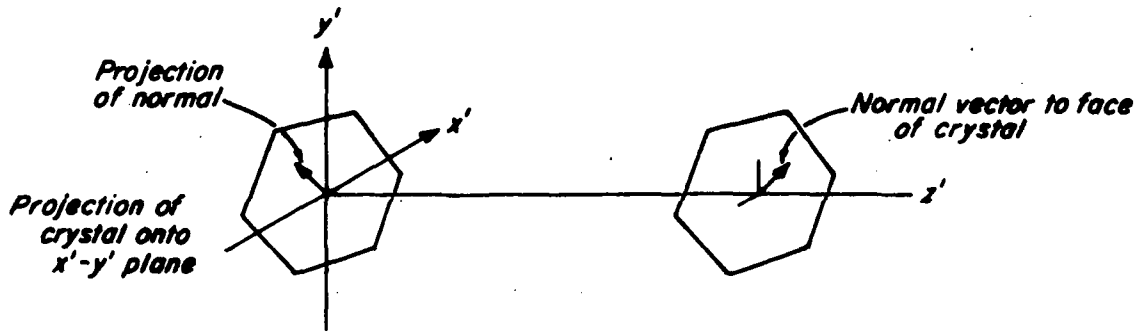
$$\Delta n = \frac{\sin^2 \theta_e}{n^2 + 2 \sin^2 \theta_e}.$$

The path length inside the crystal is  $tn / \left( n^2 - \sin^2 \theta_e \right)^{1/2}$  and thus the phase shift between the two polarizations is

$$\phi = 2\pi \frac{\delta t}{\lambda} \frac{n \sin^2 \theta_e}{(n^2 + 2 \sin^2 \theta_e)(n^2 - \sin^2 \theta_e)^{1/2}} \quad \text{in radians.}$$

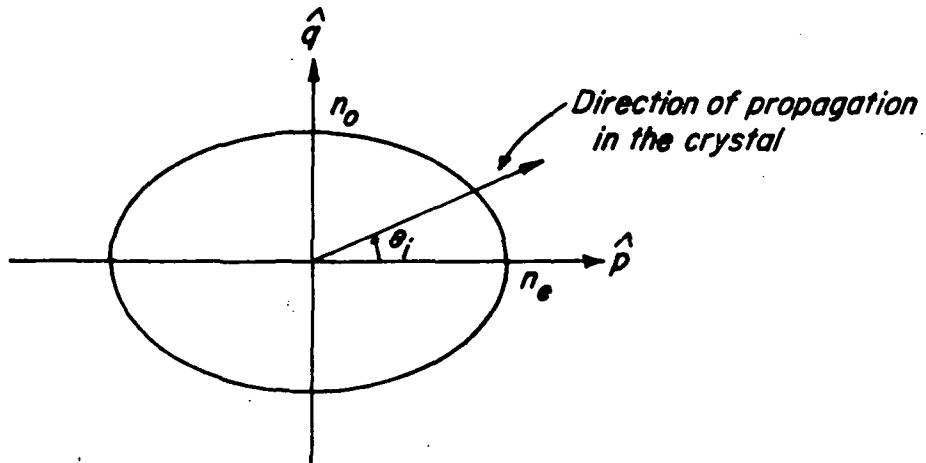
At  $\lambda = 0.6328 \mu$ , for  $t = 226 \mu$ ,  $2\pi \frac{\delta t}{\lambda} = \frac{\pi}{2}$  (see [1], p. 45).

For the given orientation, if power  $P$  enters the crystal, the power carried by the transmitted waves with polarization perpendicular to the incident polarization is  $P \sin^2 \phi/2$ .



607121

Figure 2-3 Geometry of Case 1



607122

Figure 2-4 Cross Section of the Index Ellipsoid of a Uniaxial Crystal

This power is now taken as flowing through a circular region of diameter  $d$  in a plane immediately behind the crystal. The diffraction pattern of this radiation varies as  $(J_1(k a w)/k a w)^2$ , where  $k = 2\pi/\lambda$ ,  $a = d/2$  and  $w$  is the angle through which the power is diffracted. In this case, a quantity of interest is the fraction of the total power that is diffracted at angles  $w > w_0$ . This is, [4],  $J_0^2(k a w_0) + J_1^2(k a w_0)$ . To evaluate this more conveniently, the approximation in [5] is used.

$$J_n(z) \sim \left(\frac{2}{\pi z}\right)^{1/2} \cos\left(z - n\frac{\pi}{2} - \frac{\pi}{4}\right)$$

$$\text{Thus, } J_0^2(k a w_0) + J_1^2(k a w_0) \sim \frac{2}{\pi k a w_0}$$

Figure 2-5 shows a comparison of the function and the approximation. As can be seen, the accuracy of this approximation is excellent for  $k a w_0 > 2$ , and even for  $k a w_0 = 1$ , it is consistent with the intended use of these calculations.

In the case of this ice particle counter, the mask shown in Figure 2-2 has an inner zone, completely opaque, of radius 0.013 radians, and its outer radius is 0.055 radians, both angles being measured from the center of the scattering volume. In the region where it transmits light, the open part is 1/9 of the total area. Thus, of the diffracted power, the mask collects a fraction

$$\frac{2}{9\pi^2} \times \left(\frac{1}{0.013} - \frac{1}{0.055}\right) \frac{\lambda}{d} = 1.32 \frac{\lambda}{d} = \frac{0.84}{d}, \text{ } d \text{ in microns.}$$

This estimate is expected to be valid for  $d > 15.5\mu$ , corresponding to  $k a w_0 = 1$  at the inner radius of the mask.

The total power intercepted by the particle is  $P_0 \frac{\pi}{4} d^2$ , where  $P_0$  is the power density per unit area at the center of the laser beam.

In this instrument, the laser has  $10^{-3}$ W power output in a Gaussian beam with a diameter of  $1040\mu$  at the  $1/e^2$  points, and thus  $P_0 = 2.5 \times 10^{-9} \text{ w}/\mu^2$ .

To prevent the unpolarized plasma light from the laser from creating noise in the detected signal, the laser beam passes through a polarizer before entering the scattering volume. This polarizer has a transmission of approximately 0.5, as does the polarizer located in front of the detector, which is used to separate the cross polarized component of the scattered light. Also, there is an interference filter located in front

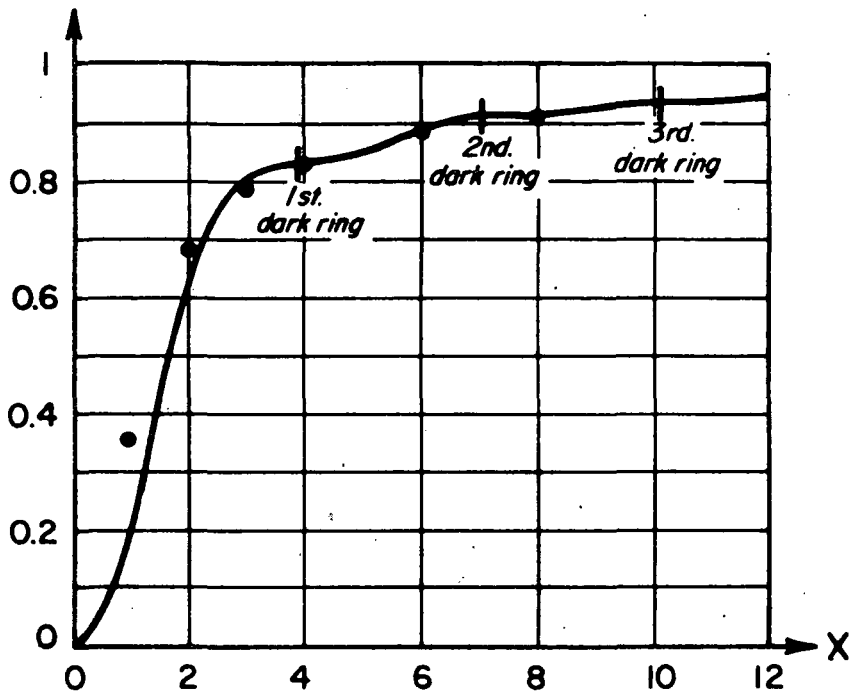


Figure 2-5 Function  $1 - J_0^2(x) - J_1^2(x)$  Representing the Fraction of Total Energy<sub>0</sub> Contained within Circles of Prescribed Radii in the Fraunhofer Diffraction Pattern of a Circular Aperture Points show the approximation  $1 - 2/\pi x$ .

of the phototube, and this, too, has a peak transmission of 0.5. These losses result in an effective value of  $P_0$  of  $3.2 \times 10^{-10} \text{ w}/\mu^2$ .

When the normal to the surface of the plate is at an angle  $\theta_e$  to the beam, the projected area of the particle is reduced by  $\cos \theta_e$ ; the detected power will not decrease by this amount, because the fraction of the diffracted light that passes the mask increases, but exact fraction would be very difficult to calculate because the isophotes of the diffraction pattern are elliptical, while the boundaries of the mask remain circular and radial. Instead, note that if the projected outline of the particle were compressed by a factor  $\cos \theta_e$  along both axes, this would be just a decrease in  $d$  by that factor. The diffracted power would decrease by  $\cos^2 \theta_e$ , but the fraction collected would increase by  $1/\cos \theta_e$ , for a net decrease of  $\cos \theta_e$ . Thus, we approximate the decrease in detected signal as  $\sqrt{\cos \theta_e}$ , for this case in which the projected outline is compressed along only one axis.

The previously calculated expression for  $\phi$  may be rewritten as

$$\phi = \frac{t}{144\mu} f(\theta_e, n) \quad \text{where } f(\theta_e, n) = \frac{n \sin^2 \theta_e}{(n^2 + 2 \sin^2 \theta_e)(n^2 - \sin^2 \theta_e)^{1/2}}$$

The purpose of the present computations is to obtain a comparison with the measured pulse heights observed during the calibration tests described later. In those tests, the ice crystals were generated in a cold chamber and simultaneously with the measurements by the ice particle counters, formvar replicas of the crystals were made. For somewhat less than 1 percent of the platelets captured, it was found that two had clumped together before capture, so that one formed a replica of a vertically oriented platelet, for which both thickness and diameter could be measured. The average ratio of thickness to diameter measured for these was 1/6. Since the largest particles observed were only about  $200\mu$  in diameter, and since  $f(\theta_e, 1.3)$  is always  $<1$ , it is evident that  $\phi$  is always small enough that  $\sin^2 \phi/2 \sim (\phi/2)^2$ .

Thus, the detected power is

$$\begin{aligned} P_{\text{det}} &= (3.2 \times 10^{-10}) \left(\frac{\pi}{4} d^2\right) \left(\frac{0.84}{d}\right) \left(\frac{t}{288}\right)^2 f^2(\theta_e, 1.3) \sqrt{\cos \theta_e} \\ &= 2.1 \times 10^{-10} d \left(\frac{d}{1728}\right)^2 f^2(\theta_e, 1.3) \sqrt{\cos \theta_e} \\ &= 7 \times 10^{-17} d^3 f^2(\theta_e, 1.3) \sqrt{\cos \theta_e} \end{aligned}$$

Figure 2-6 is a graph of  $f^2(\theta_e, 1.3) \sqrt{\cos\theta_e}$ . As can be seen, this function has a maximum value of approximately 0.08, at  $\theta_e = 70^\circ$ . Thus, finally, the maximum detected power is estimated to be

$$P_{\text{det}} = 5.6 \times 10^{-18} d^3 \text{ watts, } d \text{ in microns.} \quad (1)$$

Note that this assumes  $t/d = 6$ .

#### 2.4 Case 2: Small, Short Column

The prototype crystal for this case is a plate in which  $t = d/2$ , so that the facets parallel to the optical axis are squares of side  $d/2$ . The formula derived above can be applied here, but with  $t$  replaced by  $d$ ,  $d$  replaced by  $d/2$ , and the terms involving  $\theta_e$  deleted. The maximum signal occurs when the optical axis is perpendicular to the laser beam and at  $45^\circ$  to the incident polarization. The detected power is

$$\begin{aligned} P_{\text{det}} &= (3.2 \times 10^{-10}) \left(\frac{\pi}{10} d^2\right) \left(\frac{1.68}{d}\right) \left(\frac{d}{288}\right)^2 \\ &= 1.3 \times 10^{-15} d^3 \end{aligned} \quad (2)$$

#### 2.5 Case 3: Large or Very Birefringent Column with $t \sim d$

In this case, the same formula as in Case 2 applies, but the term  $(d/288)^2$  is deleted, since now it is assumed that  $\phi$  is large, and instead of  $\sin^2\phi/2 \sim (\phi/2)^2$ , the appropriate approximation for finding the maximum pulse amplitude is  $\sin^2\phi/2 \sim 1$ .

$$P_{\text{det}} = 1.05 \times 10^{-10} d \quad (3)$$

#### 2.6 Case 4: Column with $t \gg d$ and Smooth Facets

In this case  $t$ , which is the length of the column, is large compared to the diameter and as a result the diffraction pattern is elongated as shown in Figure 2-7.

Without actually evaluating the required integrals, we may note that the width of the diffraction pattern,  $w$ , varies as  $1/t$ . Consider a point in the plane of the mask, located at a distance  $u$  from the centerline of the diffraction pattern and at a distance  $v$  from the center of the pattern along the perpendicular direction. At that point, the electric field intensity varies as  $u/w$ , the power density varies as  $(u/w)^2$ , and thus

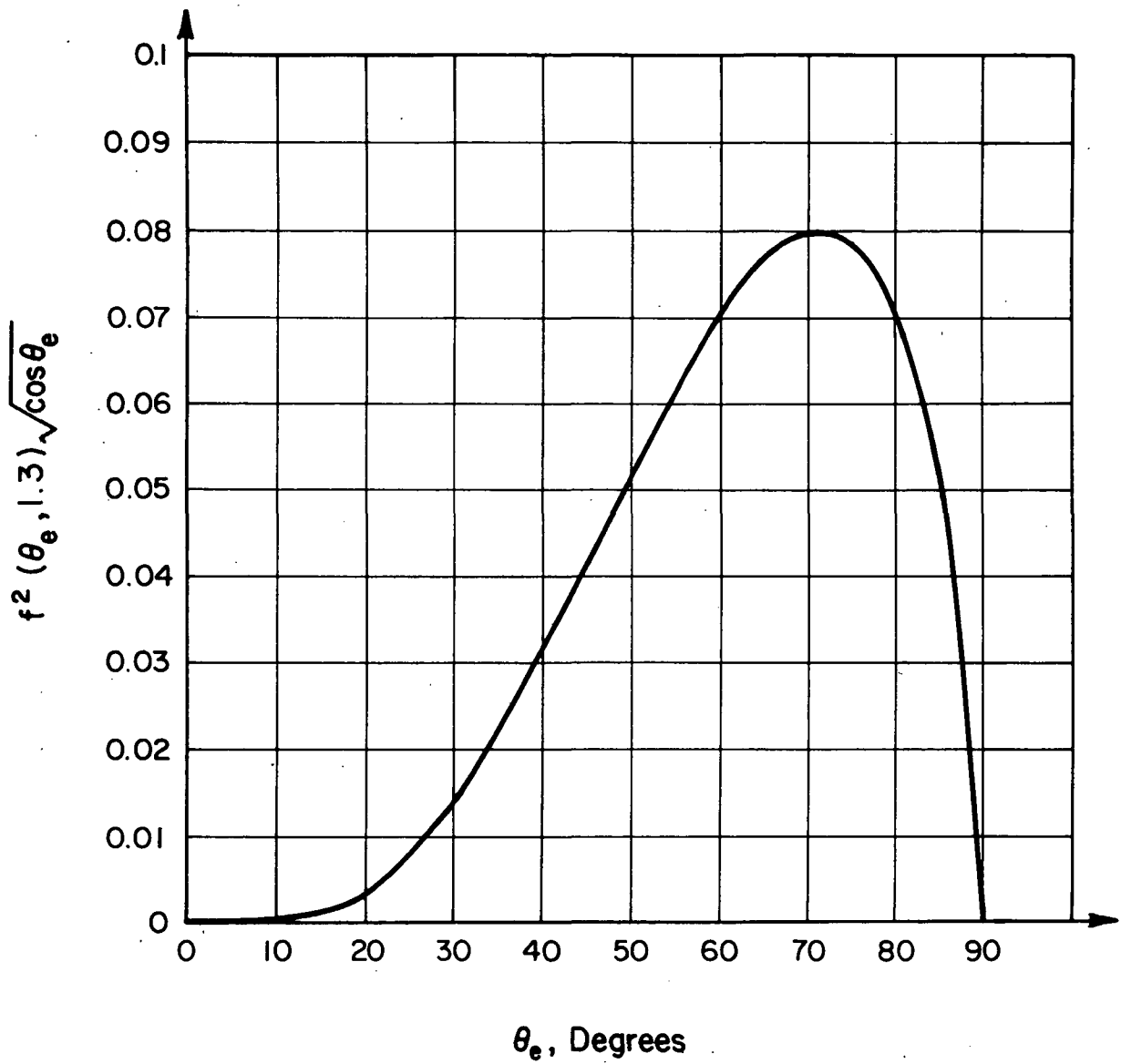


Figure 2-6 Graph of  $f^2(\theta_e, 1.3) \sqrt{\cos \theta_e}$

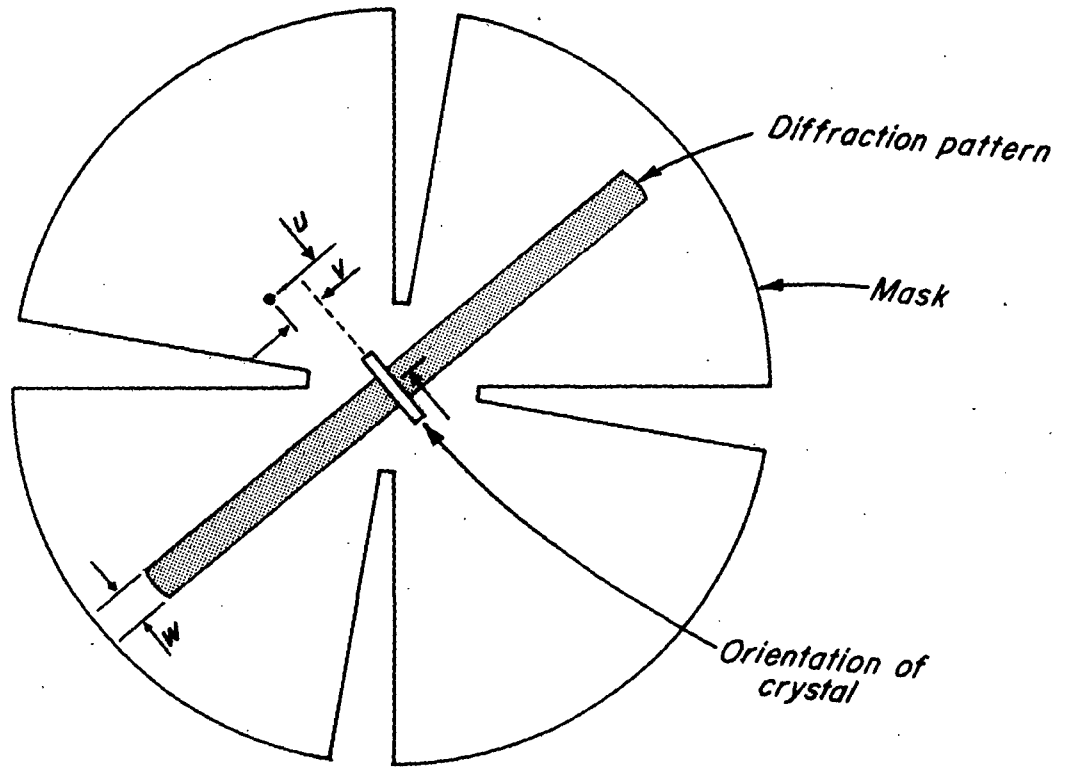


Figure 2-7 Diffraction Pattern of Columnar Ice Particle

the fraction of the power intercepted by the open parts of the mask varies as  $1/w$ . The total diffracted power is proportional to  $w$ , however, and thus the detected power should be independent of  $w$ , and thus of  $t$ . Hence, the formulas of Cases 2 and 3 continue to apply.

Note, however, that the above result presupposes that a uniform wavefront is transmitted by the crystal. In macroscopic crystals, a long column of this sort would seldom have perfectly flat faces. Instead there would be striations and irregularities in its growth along the length of each facet. This might also occur in the case of ice crystals, and the same effect could also arise from faults or impurities located along the center line of the column.

If the facet is divided into a number of locally flat regions, each occupying the full width of the facet and of length equal to the width, and if the transmitted wavefront shows an rms variation of  $\pi/2$  or more from one region to the next, then the diffraction pattern will be a spatially incoherent superposition of the diffraction patterns of the individual regions; thus, Case 5 arises.

## 2.7 Case 5: Column with $t \gg d$ and Rough Facets

The formulas of Case 2 and Case 3 continue to apply, but in each case the total power detected is multiplied by  $t/d$ , the number of locally flat regions on the facet, and for small columns

$$P_{\text{det}} = 1.3 \times 10^{-15} d^2 t \quad (5a)$$

while for large and/or highly birefringent columns

$$P_{\text{det}} = 1.05 \times 10^{-10} t \quad (5b)$$

Although it is quite likely that this kind of surface roughness effect plays a role in the scattering of light from most ice crystals, it also introduces an arbitrary parameter into the calculations: the size of the locally flat regions. Also, although the surfaces of the platelets used in the calibration had irregularities, as seen in the formvar replicas, the columns formed in these tests had smooth, flat faces, as well as could be seen at 400x magnification.

All of the scattering mechanisms considered above use only the birefringence of ice to change the polarization of the incident light. This depolarization can also be caused by internal reflection. Since this depolarization occurs after a single bounce, it might be expected to be especially important for small ice crystals. To be effective, this mechanism requires that: 1) most of the light entering the crystal must be internally reflected at least once; and 2) the scattered light must remain near the axis of the incident beam; these conditions are met in the case of columns with  $t \gg d$ , and in plates with  $t \ll d$ , but not for short columns (or thick plates) with  $t \sim d$ .

#### 2.8 Case 6: Internal Reflecting Column with $t \gg d$

In this case, the axis of the column is at an angle  $\theta$  from the direction of the incident light. The light transmitted from the other end is more or less uniformly distributed in a cone of semi-angle  $\theta$  centered about the particle's axis. Thus, the light reaches the mask as shown in Figure 2-8.

The width of the ring,  $W$  in this figure, is the diameter of the diffraction pattern corresponding to the cross section of the particle. As can be seen from the figure, the fraction of the scattered light transmitted by the mask will not depend strongly on  $W$ . In the case shown, the open area of the mask has length  $2\theta \cdot \frac{2\pi}{36}$  while the circumference of the pattern is  $2\pi\theta$  and thus the fraction of the light collected is  $1/18$ . Thus,

$$\begin{aligned} P_{\text{det}} &= (3.2 \times 10^{-10}) \left(\frac{\pi}{4} d^2\right) \left(\frac{1}{18}\right) \\ &= 1.4 \times 10^{-11} d^2 \end{aligned}$$

#### 2.9 Case 7: Thin, Internally Reflecting Plate

In this case, the light enters one edge of the crystal in a direction nearly parallel to the face, and travels by internal reflection to the opposite edge. Both irregularities in the edges and variations in the thickness of the plate will cause nonuniformities in the transmitted wavefront, and thus formula (5b) applies in this case also, with  $t$  replaced by  $d/2$ .

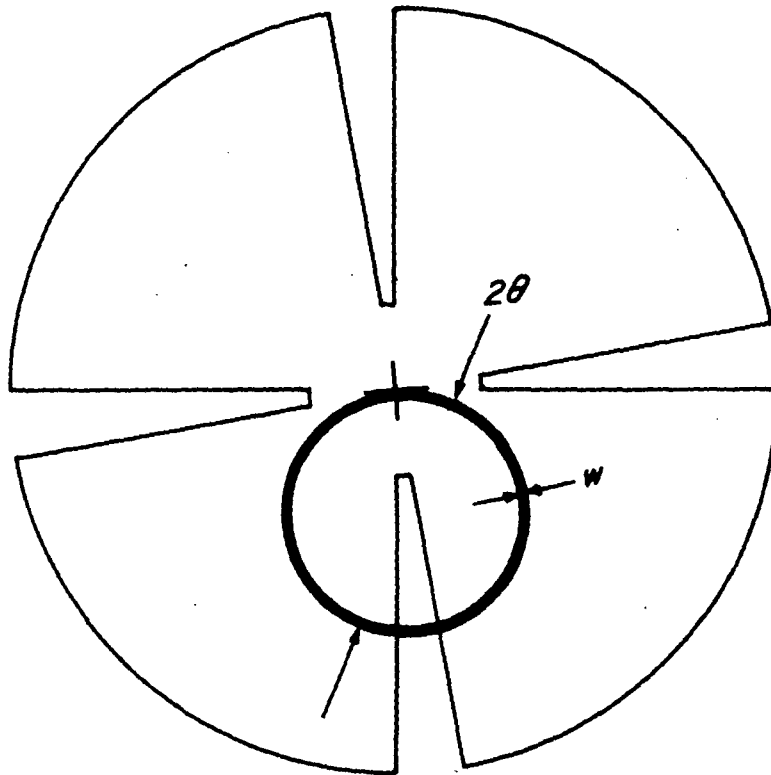


Figure 2-8 Scattering into Mask Plane from Internal Reflecting Column with  $t \gg d$

All of the above calculations have assumed that the light is scattered by diffraction alone. If the surface of the crystal is somewhat rough (e.g., rimed crystals) there will be two effects: for large crystals, a large fraction of the light will be scattered far enough off axis to be detected, thus causing a larger signal than calculated, and for all crystals there will be a reduction in signal due to light scattered at large angles, and thus not detected. These effects have not been included in the calculations because to do so would have required a detailed knowledge of the scattering law of the surface irregularities.

In the case of scattering mechanisms involving internal reflection, surface roughness also causes the loss of light by permitting some of the light to escape where it should have been internally reflected. This effect is likely to be especially significant in the case of internally reflecting plates, since plates usually, except very small ones, have irregularities on their surfaces.

### 3. MECHANICAL DESIGN

Figures 3-1 through 3-5 show the construction of the ice particle counter. In these figures, the heaters used to keep the laser in its operating temperature range have been removed to better show the rest of the structure.

The laser used is a Hughes model 3180H, which provides 1 mw nominal power output. This laser was selected for its small overall length and 1000:1 polarization of its output. A polarizer is attached to the front of the tube to polarize the incoherent radiation from the plasma tube. The power output is monitored by measuring the output from the rear mirror, which transmits a few tenths of 1 percent; this light goes through a red plastic filter and then falls on a silicon photocell, which is held by part number 1, depicted in Figure 3-3.

The laser slides into a slightly oversized hole in the main spar of the instrument, part number 2 of Figure 3-3. At its front end, it is kept centered by an O-ring, while the rear end is held by the split and threaded end of the spar, which is closed onto the laser by a clamp ring, part number 3 of Figure 3-3.

As shown in Figure 3-2, the power leads to the laser pass through a slot in the wall of the spar. This slot is widened at the end to permit the plane of polarization of the laser to be adjusted over the range of a few degrees. That is, the polarizer associated with the phototube is fixed, and the orientation of the laser is adjusted to make its polarization exactly perpendicular to that of the phototube's polarizer.

The 7 ma, at 1050v, operating current of the laser is supplied by a dc-dc converter, part number 4 of Figure 3-3. This converter runs from 12v, 1.7A dc. This arrangement has several advantages, especially in that it avoids the need to carry high voltage via a long cable run, and the power dissipated in the supply serves in part as a heat source to keep the laser in its operating range, -20°C to +50°C.

Also shown in Figure 3-3 are part number 5, the web that spaces the spar with respect to the outer shell, and part number 6, a bakelite spacer ring. The purpose of the spacer ring is to reduce the otherwise large heat loss that would occur by conduction through the web. The

1. Long Allen Wrench, 7/64", for installation of Phototube
2. Allen Wrench, 5/16"
3. Allen Wrench, 9/64"
4. Allen Wrench, 7/64"
5. Allen Wrench, 5/64"
6. Long Allen Wrench, 9/64", for installation of Phototube clamp ring
7. Screwdriver
8. Spanner Wrench to install laser power monitor diode
9. Threaded rods for installation of backup ring under Phototube web
10. Alignment screws and keeper nuts
11. Spanner Wrench for laser clamp ring
12. End plate
13. Outer shell
14. Mounting flange
15. Sampling tube
16. Inlet fairing

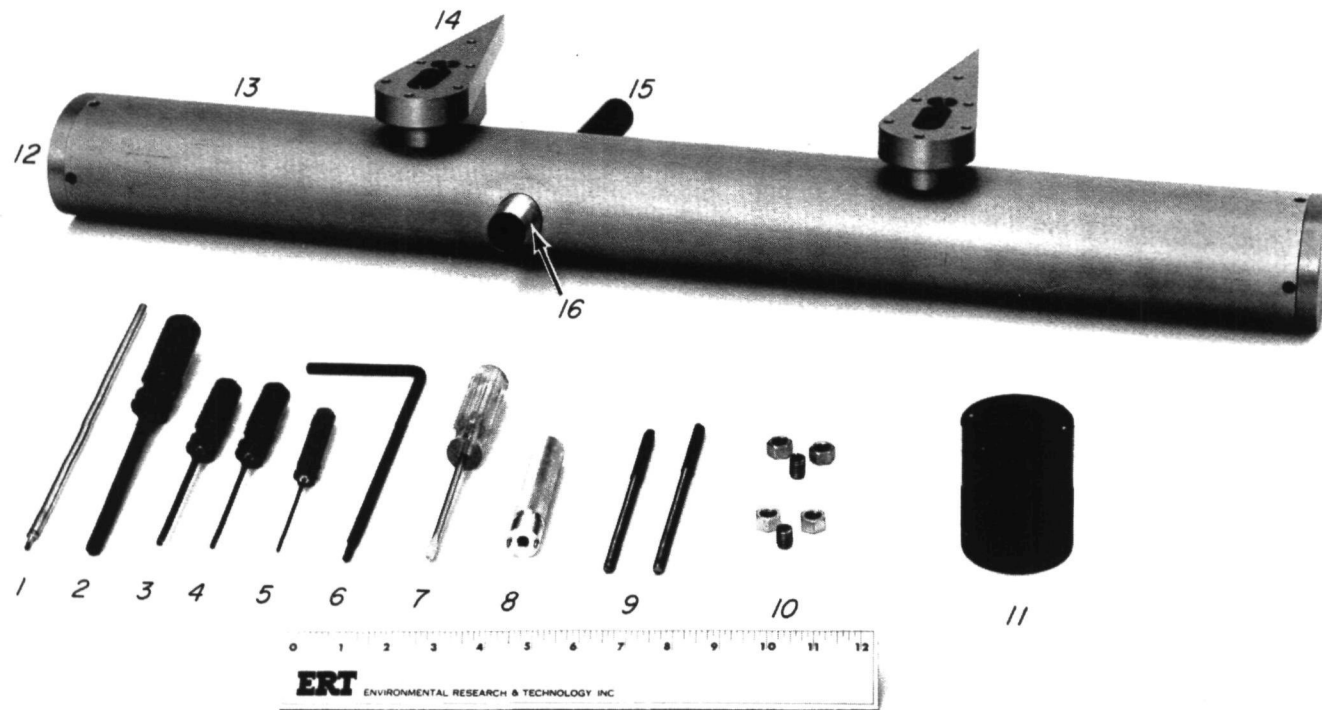


Figure 3-1 Assembled View of Ice Particle Counter; Tools for Assembly and Disassembly

1. Laser web
2. Phototube web
3. Main spar
4. Sampling tube
5. Laser web spacer ring
6. Extension sleeve spacer ring
7. Extension sleeve
8. Slot for laser leads
9. Outer shell
10. Mounting flange, assembled with keeper nuts
11. Mounting flange, disassembled
12. Inlet fairing
13. End plate
14. Phototube
15. Laser clamp ring

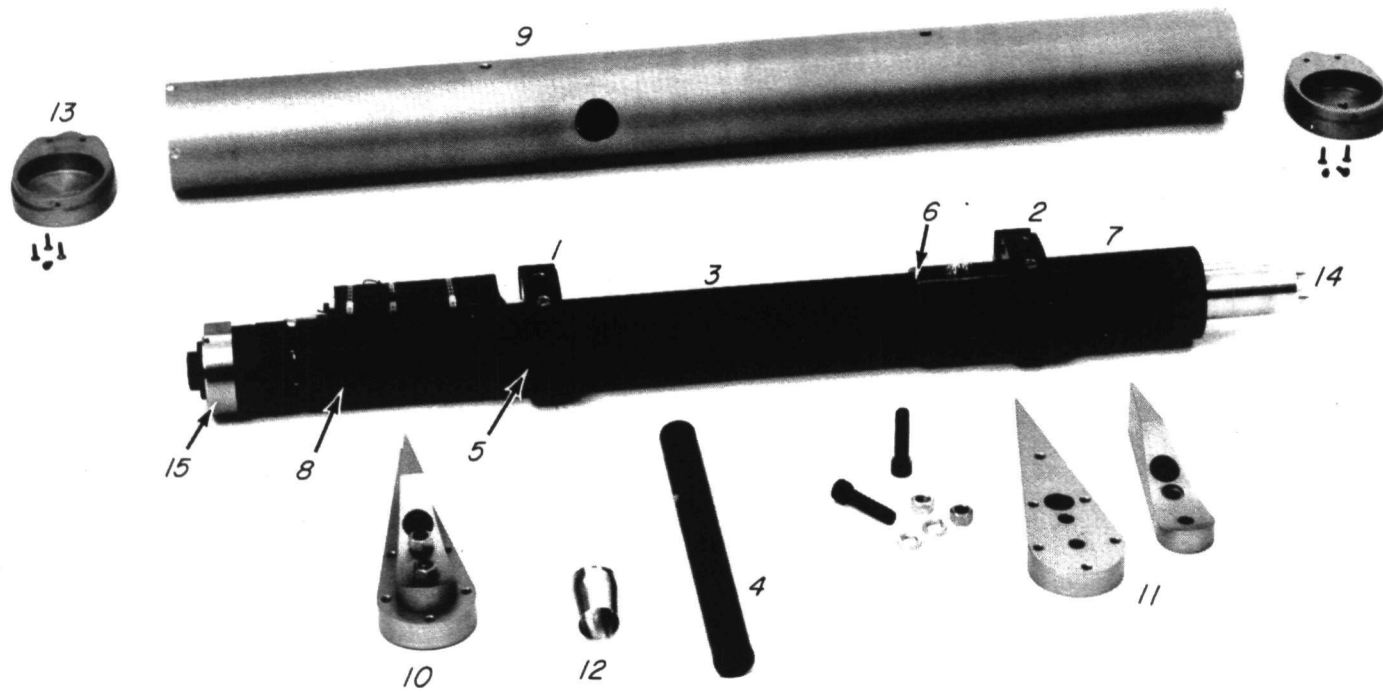


Figure      Ice Particle Counter -- Disassembled

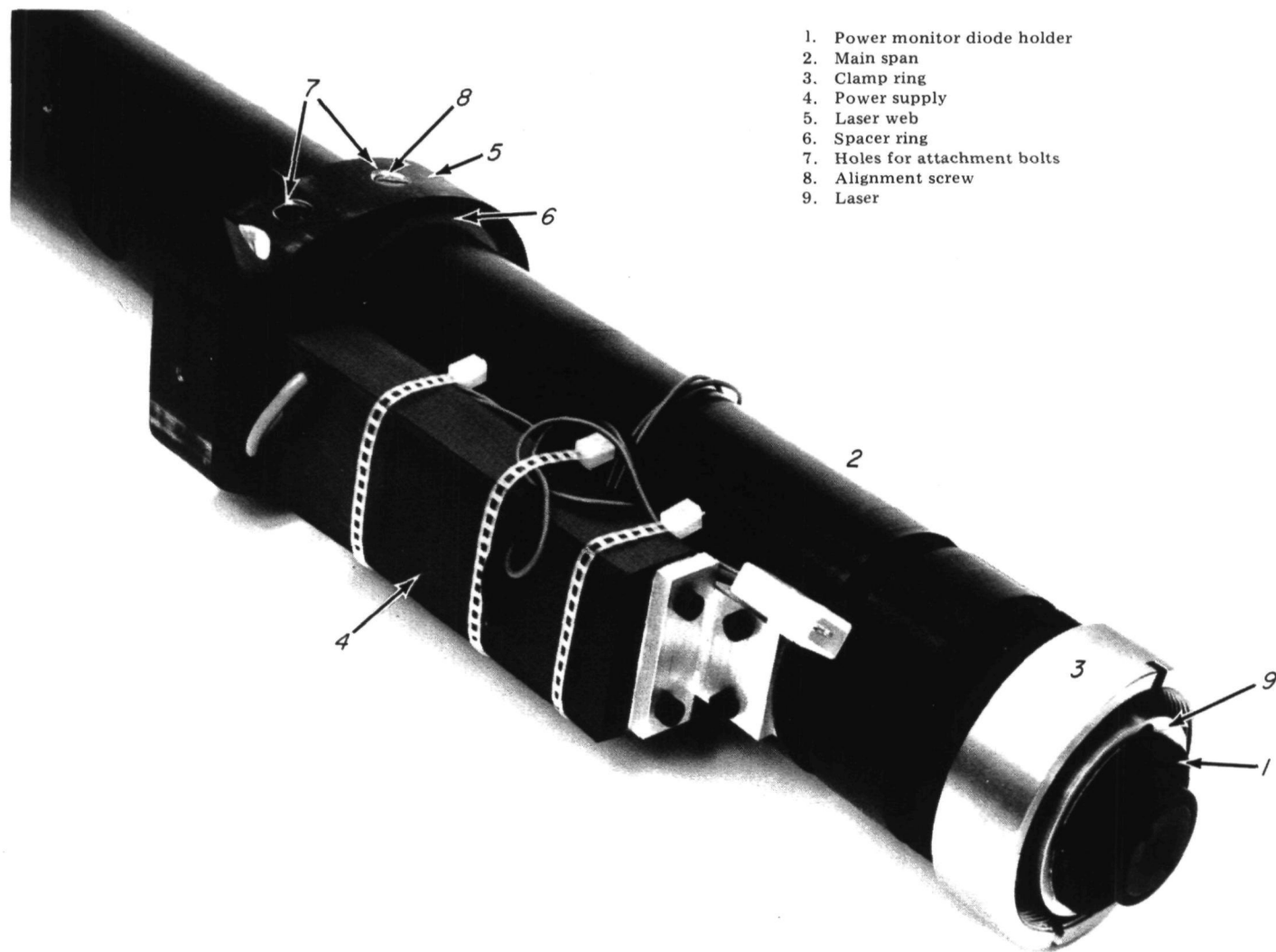


Figure 3-3 Detail of Laser

1. Phototube
2. Clamp ring
3. Hole for bolt used in removing clamp ring
4. Extension sleeve
5. Phototube web
6. Extension sleeve spacer ring

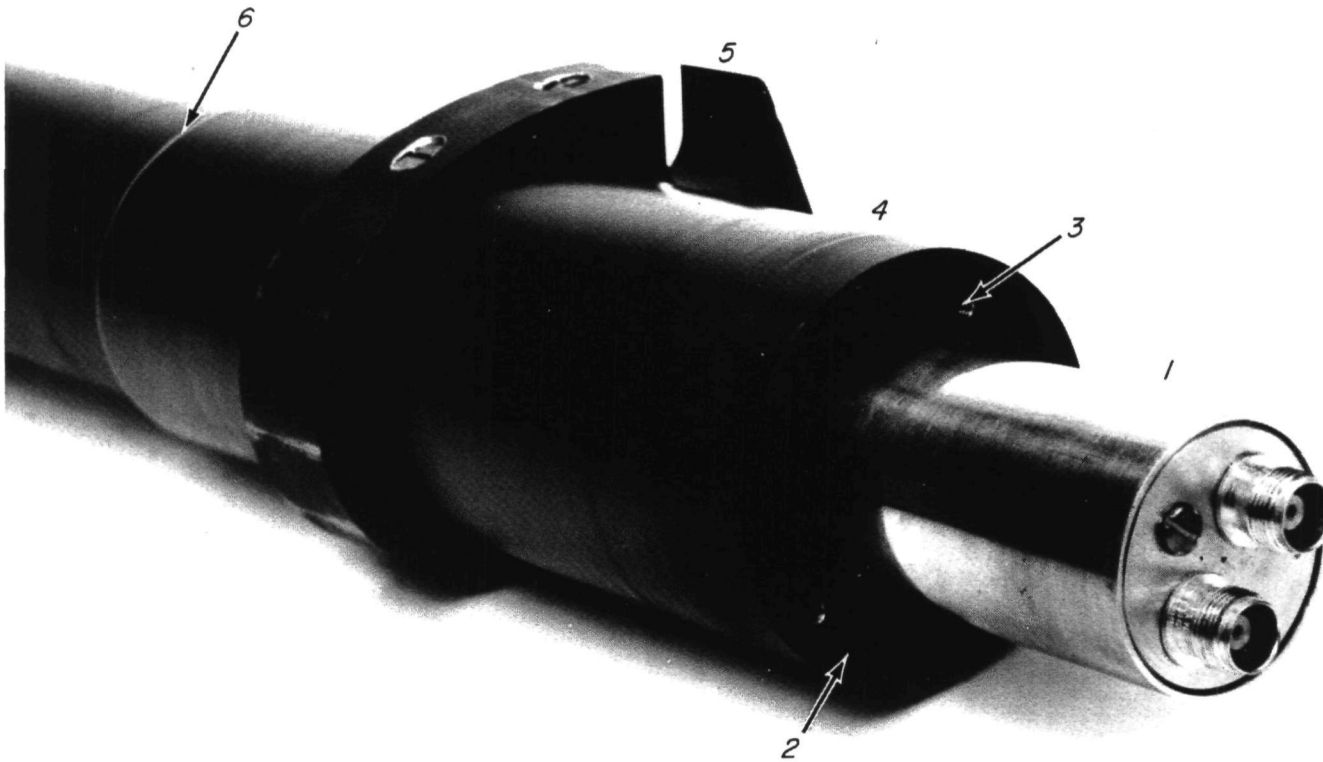


Figure 3-4 Detail of Phototube

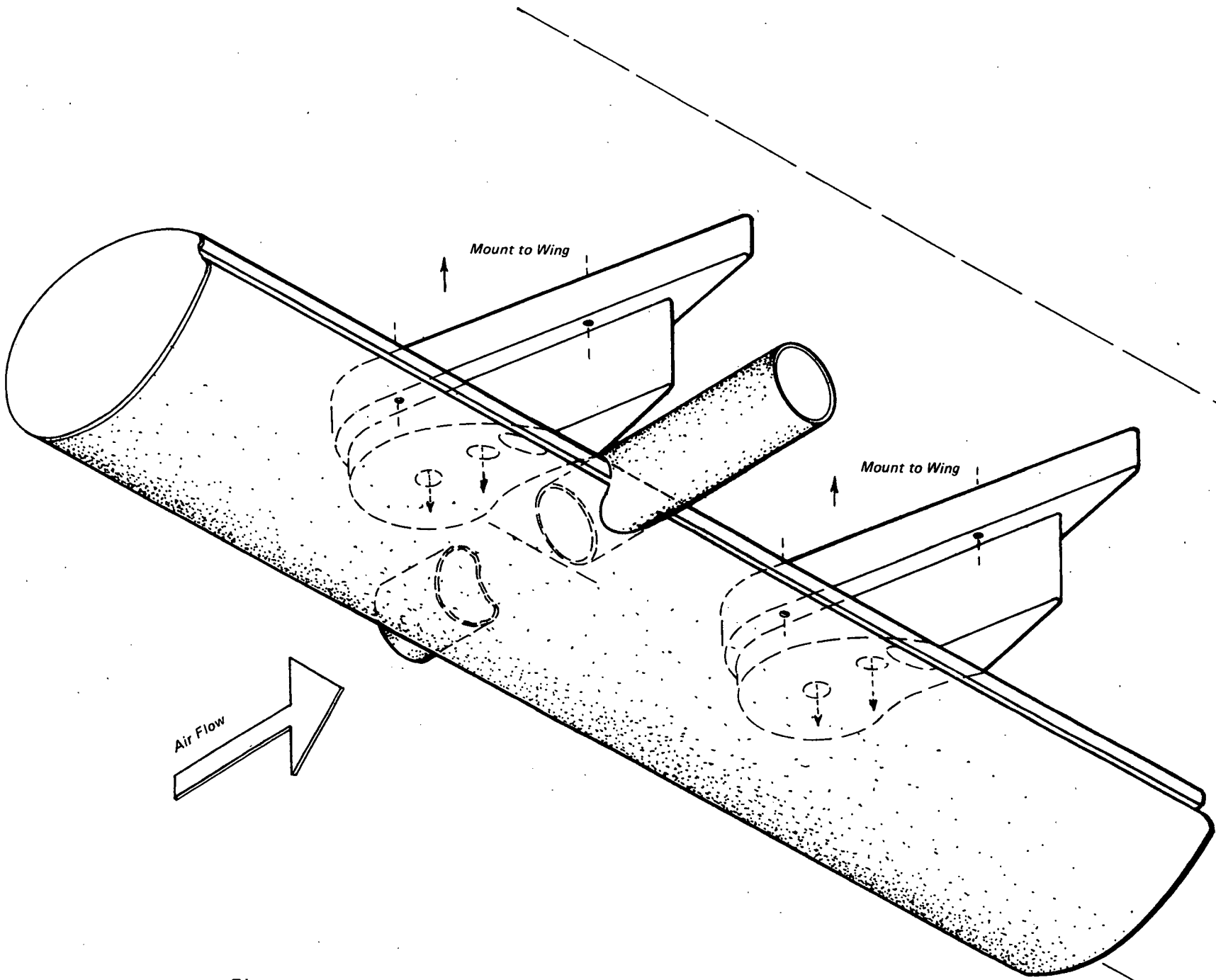


Figure 3-5 Ice Particle Counter as Mounted to an Aircraft

outer shell and the spar inside it are attached by two 3/8-16 bolts into each of the webs. At the laser end, the rear bolt goes into the web only, while the front bolt enters into the 1/4" wall of the spar. This bolt is the only direct path for heat loss; if a stainless steel bolt is used, the total conduction loss (through the bolt, plus conduction through the spacer ring) will be about 40w for a spar temperature of +20°C and an ambient temperature of -50°C.

The bolts fit into the holes marked 7, which are shown in Figure 3-3. In the forward hole, there is an alignment screw, 8, that keeps the web from slipping when the instrument is disassembled. This alignment screw is removed before placing the bolt in its proper position.

The scattering volume is the region where the laser beam, which coincides with the spar axis, passes through the sampling tube, which is part number 4 of Figure 3-2. Before entering the sampling tube, the laser beam passes through two circular apertures, which block multiple reflections from the face of the polarizer and also some of the incoherent light from the plasma tube. On leaving the sampling tube, the laser beam and any scattered light pass through three more circular apertures, which serve to block any ambient light which might otherwise reach the phototube via the sampling tube.

The end of the main spar is located 8" from the centerline of the sampling tube, and the phototube assembly, which has a flange, bolts onto this end. Clamped between the flange and a shoulder on the main spar is another bakelite spacer ring (part number 6 of Figure 3-2) which is in turn pinned to an extension sleeve, part number 7 of Figure 3-2. Near the middle of this is a second web, part number 2 of the same figure. Since the wall of the extension sleeve is relatively thin, the forward attachment bolt at this end passes through the sleeve and into a backup ring, the i.d. of which clears the phototube assembly.

At the far end of the extension sleeve is a clamp assembly consisting of two rubber disks clamped between two aluminum disks. When the screws between the two aluminum disks are loose, this slides over the phototube assembly and into the extension sleeve, but once the aluminum disks are drawn together, the expansion of the rubber disks locks the end of the phototube assembly in place and prevents it from vibrating.

Since rubber is a poor thermal conductor, the phototube assembly is mostly in thermal contact with the main spar. The extension sleeve spacer ring limits conduction loss from the main spar to 17w under the same conditions as above.

Thus, conduction losses cause less than 70w heat loss. Another principal source of heat loss is caused by the high speed airflow through the sampling tube. Based on the experience of the University of Washington workers ([1], p. 56), 200 to 300w should be adequate for this; there is ample room between the webs for heater bands of this power rating.

The U. W. instrument used an 85w heater clamped directly to the sampling tube to de-ice its inlet. Since the thin (1/32") wall of the sampling tube does not conduct heat well, this ice particle counter has a tapered fairing which slides over the front of the sampling tube. This is grooved to accept a heater winding of up to about 50w capacity, which is believed to be adequate in the light of the better heat conduction that results from this arrangement.

The phototube used here is EMI type 9798; it is part of a potted assembly that includes the high voltage supply (a dc-dc converter) and the dynode chain. The front flange of this assembly has a series-V thread, by which the interference filter, mask and polarizer are attached to the phototube.

After being assembled, the main spar, webs, etc. slide into the outer shell, and the attachment bolts are put in through the mounting flanges. The assembled ice particle counter is shown in Figure 3-1, while Figure 3-5 depicts how it typically would mount to an aircraft.

The outer shell is an aluminum extrusion, and it should provide reasonably smooth airflow at low speeds. For use at higher speeds, a more elongated airfoil could be fabricated and slipped over the outer shell.

#### 4. ELECTRONICS AND SIGNAL PROCESSING

As already noted, the phototube used in the ice particle counter is equipped with a dc-dc converter and potted dynode chain. The measured gain of the tube, relative to the gain at a reference point arbitrarily taken at 7.5v supplied, is shown in Figure 4-1 as a function of the input voltage to the converter. The voltage actually applied to the dynode chain is approximately 100 times this.

The calibration ticket supplied with the phototube gives the cathode sensitivity as 133  $\mu\text{a/lm}$ ; the anode sensitivity of 200  $\text{a/lm}$  at 990v applied to the tube proper is given, corresponding to 9.9v to the converter, or as seen from Figure 4-1, a relative gain of 10. Thus, at that voltage the actual gain is  $1.5 \times 10^6$ , and at a relative gain of 1, the actual gain is  $1.5 \times 10^5$ .

A radiometric calibration is not supplied with the tube, but from the typical values supplied by the manufacturer for this cathode type, S-20, the ratio of peak sensitivity in  $\mu\text{a/mw}$  to luminous sensitivity in  $\mu\text{a/lm}$  is 0.45, and the ratio of sensitivity at 6328 A to peak sensitivity is 0.42. Thus, the cathode radiant sensitivity of this phototube is 25.7  $\mu\text{a/mw}$  at 6328 A. At a relative gain of 3, which was the case for most of the calibration tests described later, anode sensitivity was  $1.16 \times 10^4$  A/w, and thus 1  $\mu\text{a}$  corresponds to  $0.87 \times 10^{-10}$  w detected by the phototube.

Since a wide range of particle sizes and scattering mechanisms may be encountered in various measurement situations, it is convenient to provide some form of gain compression in the circuitry following the phototube. Following this, the signal pulses are compared to a threshold and counted. Figure 4-2 shows the circuit used for these functions.

Figure 4-3 shows the transfer function of the compressor-amplifier. At low input currents, the output voltage is determined by the 100K feedback resistor, with negligible conduction by the diode. Above 1  $\mu\text{a}$  input, the diode conducts, resulting in a quasi-logarithmic compression law. The break in the slope of the curve at 10  $\mu\text{a}$  is the normal result of the recombination of carriers in the space charge region of the diode at low currents. It could have been avoided by the use of a transistor

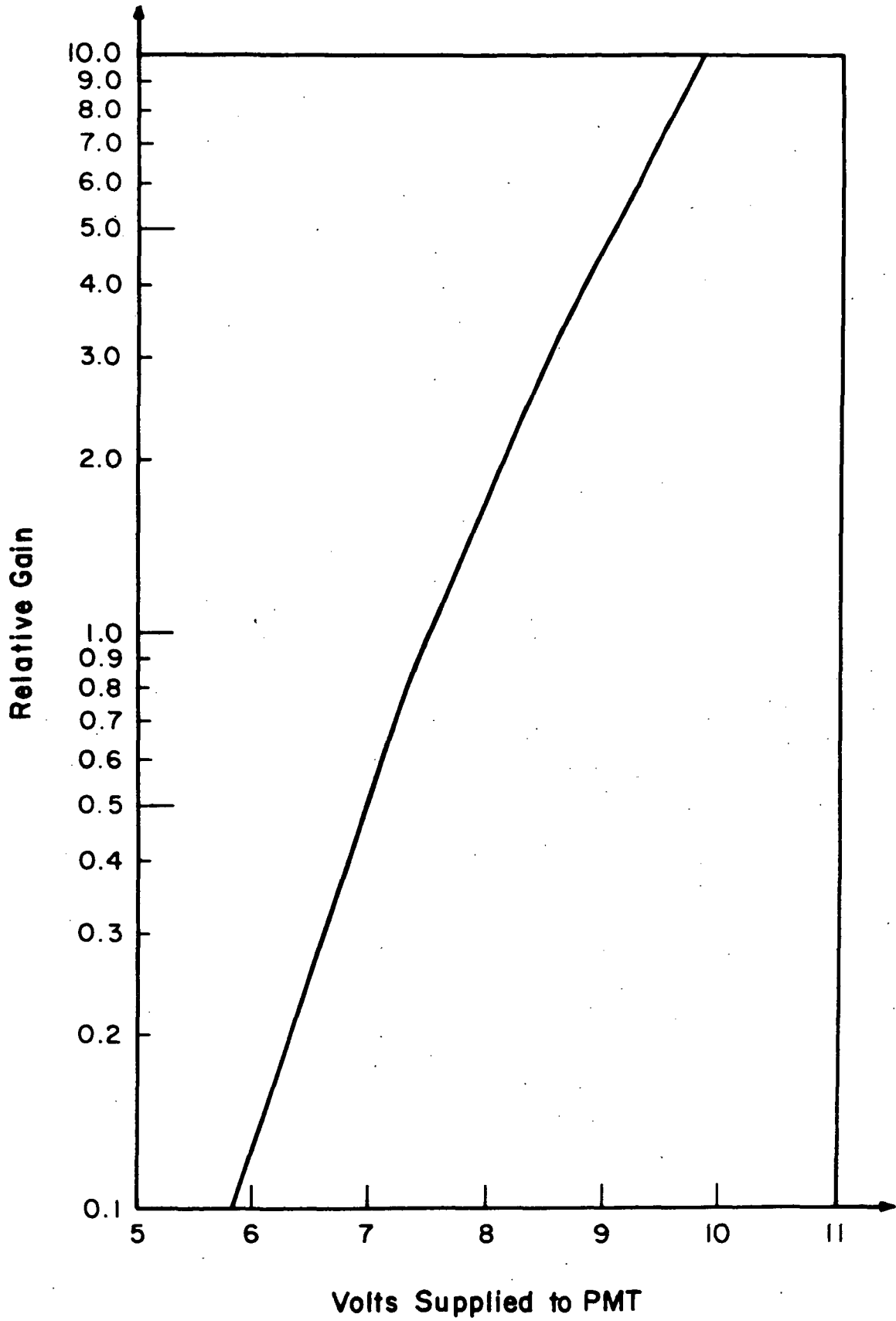


Figure 4-1 Calibration of PMT, EMI-Gencom Type MPD/IR/DCDC S/N 5799

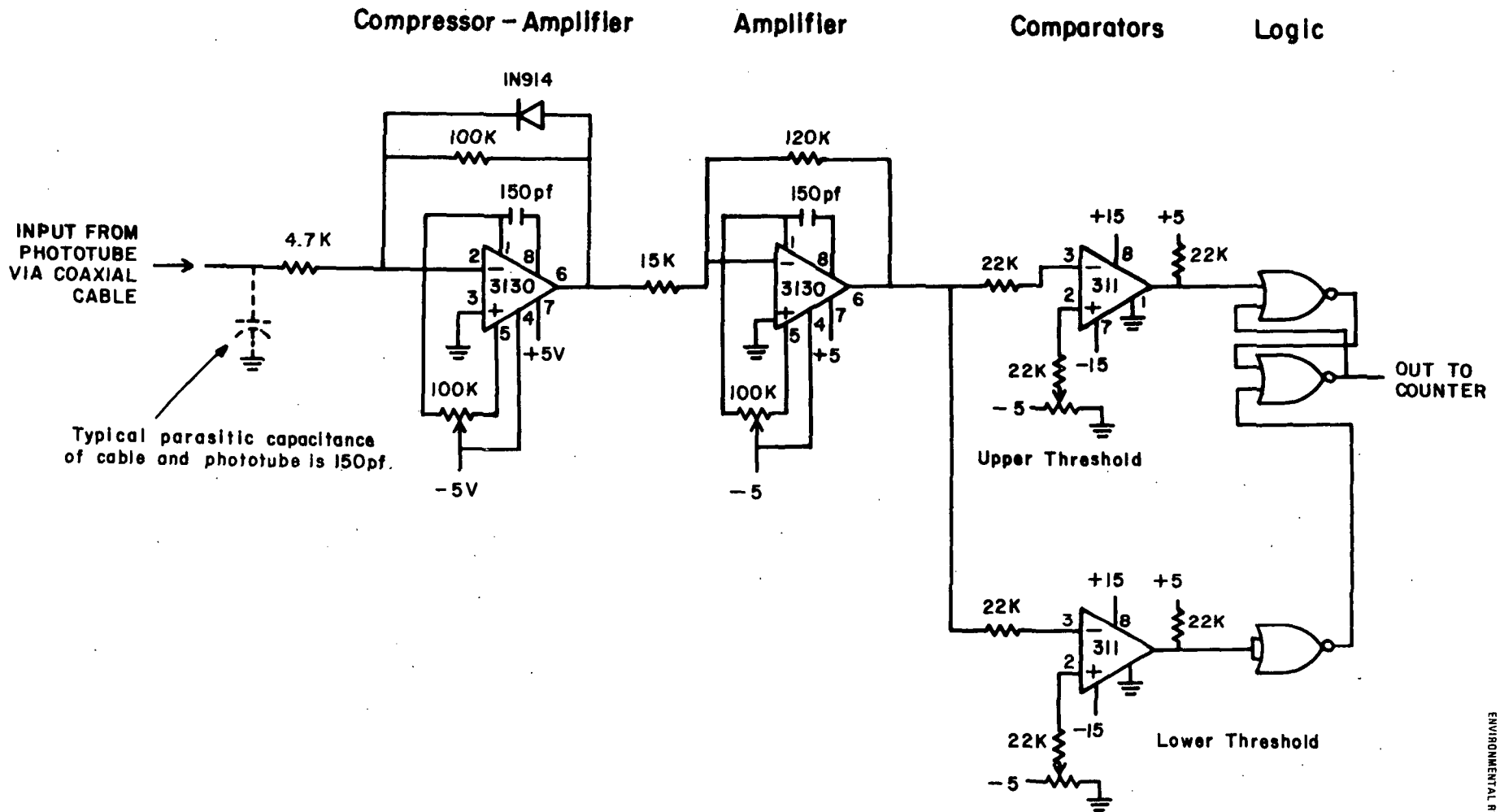


Figure 4-2 Signal Processing Circuit  
 The operational amplifiers are CA3130AT (Mfg. RCA), the comparators are LM311 (mfg. NS), and the NOR gates are CD4001AE (Mfg. RCA).

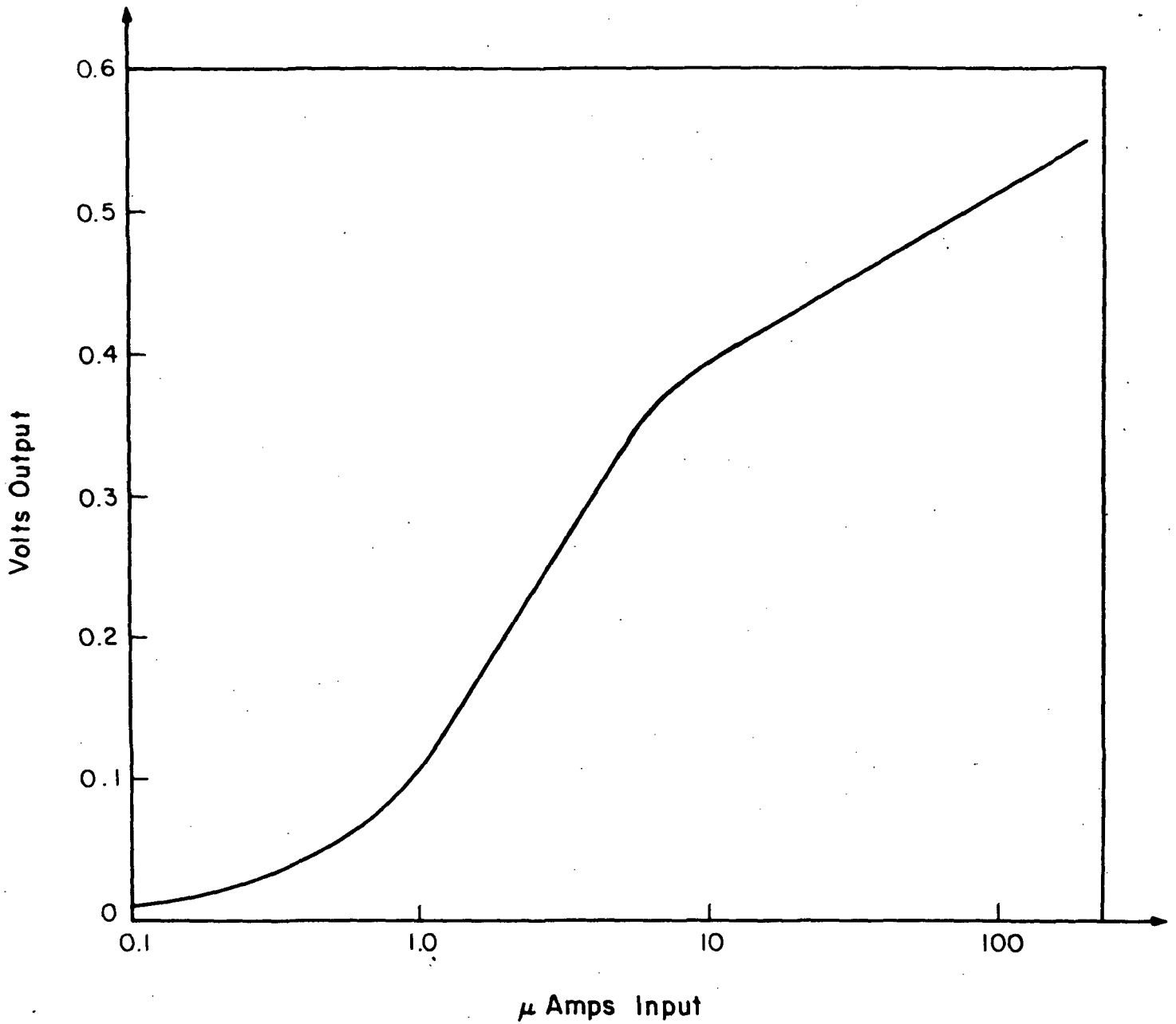


Figure 4-3 Calibration Curve of a Quasi-log Amplifier  
At low input currents, transresistance =  $10^5 \Omega$   
(V output = 0.1i input).

607137

as the feedback element, but this was not done because there was no need for a single slope -- and, in fact, the steeper slope was preferable. A transistor was also not used because the use of a diode resulted in a faster response and less of a tendency to oscillate. The 4.7K input resistor is also used to stabilize the amplifier, and has little or no effect on the transfer function. Generally speaking, current followers such as this are likely to oscillate when the source admittance is capacitive.

There are two aspects to the response speed of a circuit for this purpose: the change in maximum output when a pulse of constant input current and variable duration is applied, and the recovery time after the input pulse has returned to zero. In this circuit, for pulses larger than about 2  $\mu\text{sec}$ , the peak output voltage was essentially constant. For comparison, note that at 400 kt. airspeed, a particle requires 5  $\mu\text{sec}$  to go through the laser beam. The recovery time increased with pulse amplitude, but remained less than 10  $\mu\text{sec}$  for all input currents up to 500  $\mu\text{a}$ , which is far larger than would ever occur in normal operation. As noted in [1] (Section 6.2), dead times of this order do not degrade the data.

After another amplifier stage, with gain of 8, the signal is sent to two comparators and an R-S flipflop. An output pulse begins when the signal crosses the upper threshold, and it ends only when the signal returns below the lower threshold. Note that, since the entire detection circuit is dc coupled, there is no possibility of a threshold shift with pulse rate, until the spacing approaches the recovery time of the amplifier.

Even in the absence of any particles, there is a certain current flow and associated shot noise from the phototube. This is caused chiefly by imperfect suppression by the polarizers of incoherent light from the plasma tube. At and below room temperature, dark current from the phototube is not significant.

Because of this noise, if a single threshold were used, the instrument would often count several pulses when a single particle went through the beam. The present arrangement prevents this. It is equivalent to a

single comparator with a large amount of hysteresis (typically, the lower threshold is 50 percent of the upper threshold), and for use in a developmental instrument of this kind, the independently adjustable thresholds are a convenience.

Another advantage of this dc coupled circuit is that if an increase in the background current is caused by condensation or dirt on the laser polarizer, etc., this would be indicated by the output staying permanently high. In an ac coupled system, the same condition would only raise the noise level, thus causing spurious counting.

Because of the many complicated scattering mechanisms that can create the detected signal, ice particle counters such as the UW instrument have been used chiefly in the counting mode, that is, the signal is compared to a relatively low threshold, so that a large fraction of the particles passing through the scattering volume will be detected. The problem of detection probability has two parts: finding the optical scattering cross section for a given size and orientation of particle; and finding the effective scattering volume when particles are permitted to pass through the beam at any distance from the beam axis. The calculations of Section 2 apply to the first of these two problems; the second can be answered in some detail, since the laser beam has a Gaussian profile.

The power density at a distance  $r$  from the beam axis is

$$p = P \frac{1}{2\pi\sigma^2} e^{-r^2/2\sigma^2}$$

where  $P$  is the total power, and, for this laser,  $\sigma = 250\mu$ . Using the Cartesian coordinates shown in Figure 2-1,

$$P = P_0 e^{-(x'^2 + y'^2)/2\sigma^2} = P_0 e^{-x'^2/2\sigma^2} \cdot e^{-y'^2/2\sigma^2} .$$

Assuming that the particles are small compared to  $\sigma$ , and are moving along the  $x'$  axis, we see that the shape of the detected pulse is Gaussian, and its duration is independent of the distance  $y'$  that is the particles'

closest approach to the beam axis, and that if a given signal would have produced a peak scattered power of  $s$  by passing through the center of the beam, the actual peak signal is  $s \exp(-y'^2/2\sigma^2)$ .

From a practical point of view, the constant pulse shape is a very convenient property. It means that the user of the ice particle counter, from inside the aircraft, can determine the following.

- 1) Does the measured pulse duration agree with the known values of  $\sigma$  and true airspeed, that is, is the flow isokinetic, and does this change with yaw or changes in angle of attack?
- 2) Are all the pulses of the same width (at a fixed fraction of peak amplitude), in other words, is the flow uniform in the sampling tube?

Nonuniform flow, or a sudden change in the airspeed through the sampling tube for a given aircraft airspeed, would be a good indication of icing of the sampling tube inlet, even though this might not be directly visible from inside the aircraft.

Next, consider the case of a particle producing a signal  $se^{-y'^2/\sigma^2}$  and a detection threshold of  $s_0$ . Then the full width over which the counter will detect these particles is

$$\frac{w}{\sigma} = 2\sqrt{2 \ln s/s_0}$$

Using this, the sampling volume swept out per unit time may be calculated for any given value of  $s/s_0$ , or, equivalently, when a fixed beam diameter is used in finding the sampling volume, this gives the fraction of particles detected as a function of  $s/s_0$ . Figure 4-4 is a graph of this function. Considering it as proportional to the detection probability, this curve, with its rapid initial increase and very slow increase thereafter, is quite different from the measured detection probability curves given by Turner (ref[1], Section 4). The reason for the difference is that the measured curves apply to measurements of particles with a distribution of sizes and scattering cross sections, while the calculated curve applies to a single scattering cross section.

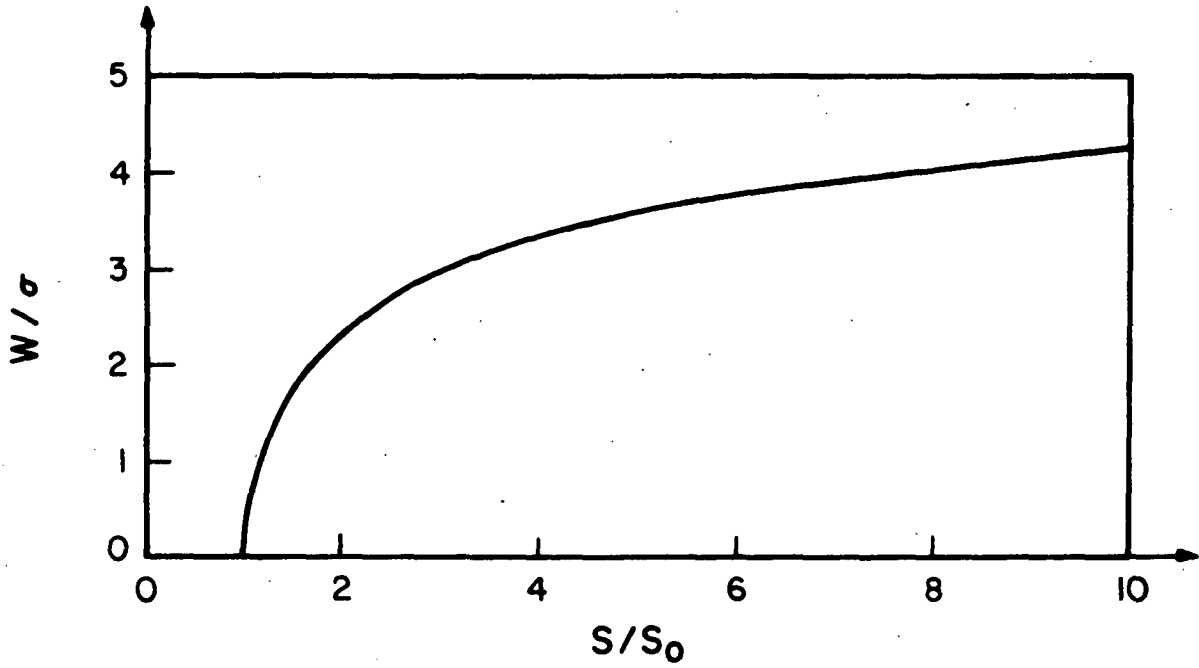


Figure 4-4 The Function  $w/\sigma = 2\sqrt{2} \ln s/s_0$

Also consider the case of pulse height analysis, in which the pulses are sorted into a series of bins in geometric progression, i.e.  $\log(\text{signal})$  is sorted into bins of uniform width, as in the GSFC Laser Nephelometer. With a normalized signal

$$S = e^{-y^2/2\sigma^2}, \text{ then } \frac{d(-\ln S)}{d y} = \frac{y}{\sigma^2} = \frac{1}{\sigma} \sqrt{-2\ln S}.$$

Changing variables to  $q = -\ln S$

$$\frac{dy}{dq} = \frac{\sigma}{\sqrt{2}} \frac{1}{\sqrt{q}}.$$

The number of particles that are detected in a given bin is proportional to the range of  $y$  that produces pulses within the bin limits. Taking these limits as  $Q$  and  $Q + \Delta Q$ , and integrating,

$$n(Q) = \int_Q^{Q + \Delta Q} \frac{\sigma}{\sqrt{2}} \frac{1}{\sqrt{q}} dq = \frac{\sigma}{\sqrt{2}} (\sqrt{Q + \Delta Q} - \sqrt{Q})$$

$$\frac{\sigma \Delta Q}{2\sqrt{2Q}} \text{ for large } Q.$$

This function decreases, though not rapidly, with increasing  $Q$ , and deconvolving it from measured pulse height spectra usually will not present any problem, especially when compared to the problem of trying to deconvolve the effects of the variable scattering cross section associated with a given size of particle.

Also, note that this formula really is accurate only in the limit of  $\Delta Q \rightarrow 0$ . Strictly speaking, it should be modified to account for the fact that not all the particles, if they passed through the beam center, would give a signal corresponding to the maximum value of one of the bins. Allowing for this would greatly complicate the analysis without adding to the understanding of the problem, so it will not be considered further.

In spite of the admitted complexity in interpreting the pulse height spectra, it seems worthwhile to plan on collecting this data, since it is entirely possible that a simple empirical correlation can be

found between pulse height data and some useful parameter such as mass or diameter distribution of the ice crystals in natural clouds. In actual use, the preamplifier and discriminator circuits described earlier must be located reasonably close to the phototube, since long cable runs carrying analog signals should be avoided where possible. If a separate discriminator were added for each bin, typically 12, as in the GSFC Laser Nephelometer, the electronics package located near the phototube would become relatively complex, and many digital signals would have to be cabled to the central processor, which is also undesirable.

A better method seems to be to add to the circuit shown a peak amplitude to pulse width converter, the peak amplitude being detected during the time that the existing circuit supplies a "1" output, and the variable width being of a pulse that starts following the fall of the existing output pulse. In this way, at the cost of a small increase in dead time (to about 20  $\mu$ sec), the data can be returned by only two digital lines. Moreover, this can be done with only two additional integrated circuits, and thus the whole circuit can be built into the base of the phototube assembly on subsequent instruments. The peak amplitude to pulse width converter has been designed but not yet built or tested.

## 5. PRELIMINARY TESTING

The ice particle counter will respond to any birefringent particle in essentially the same way that it responds to ice crystals. The use of particles of a more permanent nature than ice crystals is convenient for several reasons: the same set of particles may be used repeatedly in seeing the influence of changes in the ice particle counter's structure or alignment; the distribution of size, mass, crystal type, etc. among the particles is more easily determined; and the particles can be used for a functional test under field conditions when ice particles might not be available.

Sugar crystals were used for the preliminary testing of the ice particle counter. Although slightly hygroscopic, sugar crystals are quite suitable since they are readily available, birefringent, and as common granulated table sugar, usually have a reasonably narrow distribution of sizes. Figure 5-1 shows the measured distribution of areas for the sample used. The square root of the area gives the effective diameter of the particles, most of which had rectangular faces. As can be seen from the figure, the distribution has a cutoff point at areas of 8 to 10 x 10<sup>4</sup> μ<sup>2</sup>. A reasonable upper limit for (area)<sup>1/2</sup> is thus 3 x 10<sup>2</sup> μ.

With 6.4v supplied to the phototube, and  $G_{rel} = 0.23$  (from the calibration curve in Section 4) the voltage pulses developed across the 100k load resistor of the phototube were observed as the sugar crystals were slowly dropped through the scattering volume. The largest pulse amplitude for which a significant number of pulses occurred was 2v. This value is taken as corresponding to those crystals with (Area)<sup>1/2</sup> ~ 3 x 10<sup>2</sup> μ and optimally oriented with respect to the incident beam. Using the calibration constant of  $1ma = 0.87 \times 10^{-10} w$  at  $G_{rel} = 3$ , the measured pulse is 2.6 x 10<sup>-8</sup> w.

As seen between crossed polarizers under a microscope, the sugar crystals essentially completely depolarized the incident light. Thus, the formula derived as Case 3 of Section 2 should apply here, i.e.,

$$P = 1.05 \times 10^{-10} d.$$

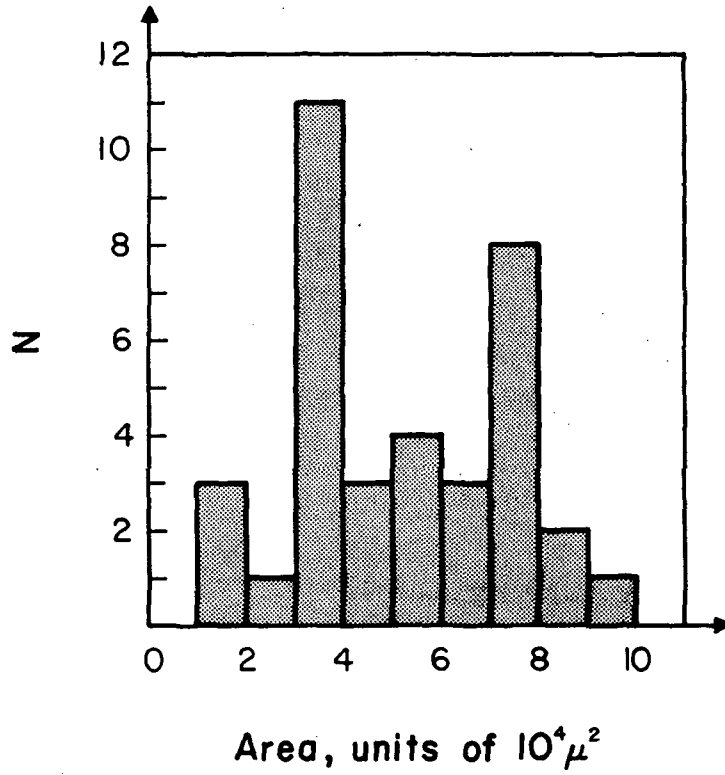


Figure 5-1 Measured Distribution of Areas of a Sample of Sugar Crystals Used in Testing the Ice Particle Counter

Using  $d = 300\mu$ , the theoretically predicted scattered power is thus  $3.15 \times 10^{-8}$  w, in excellent agreement with the measurements, especially considering that the measured cutoff point of the pulse height spectrum was only a visual estimate from an oscilloscope.

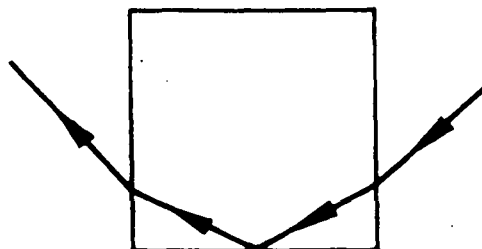
For comparison with a non-birefringent material, the pulses resulting when salt crystals were dropped through the scattering volume were observed under the same conditions as above. The salt crystals had a similar size distribution to the sugar crystals, and the pulse height spectrum showed a similar cutoff, but approximately 100 times smaller, i.e., the cutoff voltage was about 0.02v.

This rejection ratio of 100:1 is much smaller than that predicted for water drops; several phenomena may cause the signal pulses. The salt crystals were cubic, and as observed under the microscope, their surfaces had a number of small fractures especially near the edges. These fractures may have contributed some of the signal, or another source of the signal may be internal reflection, as illustrated in Figure 5-2. Rays that are only reflected once must be very close to parallel to the reflecting face or they will be deviated out of the collecting area of the phototube. For those rays that do enter at a suitable angle, only a small fraction of the light is actually reflected. The rest is simply transmitted through the opposite face of the crystal without striking the reflecting face. Moreover, light is lost from the grazing rays by the cracks and irregularities near the edges of the crystals.

Rays that internally reflect twice are transmitted parallel to the incident ray, but again this is possible only for a small fraction of the rays entering the crystal, and, as before, power is lost from these rays due to crystal imperfections.

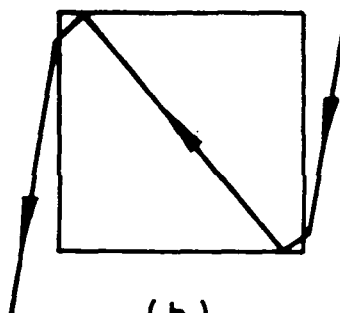
Thus, although a detailed ray trace has not been carried out, it seems that the observed small signal pulses in the case of salt grains are due to light that is internally reflected.

In another preliminary test, the ice particle counter was installed in a wind tunnel at the Naval Air Propulsion Test Center in Trenton, New Jersey. The wind tunnel was set up for use in icing tests of turbines, and was equipped with sprayers to generate a supercooled cloud of water



(a)

a. Single Reflection -- Ray is Deviated through a Large Angle



(b)

b. Two Reflections -- Ray Leaves Parallel to Incident Ray

Figure 5-2 Internal Reflection in a Cubic Crystal

drops for that purpose with temperatures of +20°F to -4°F and a nominal drop diameter of approximately 25 $\mu$ . The objectives of the test were to gain some experience in using the ice particle counter under realistic conditions, and to use it to estimate the fraction of the supercooled drops that froze before reaching it.

Since the circuitry described in the previous section had not yet been built at the time of these tests, the signal from the phototube was fed directly to a chart recorder. Since the time constant of this was long compared to the time required for a particle to go through the scattering volume, the recorded voltage was proportional to the product of the number density of ice particles and the average peak voltage produced by each. In initially evaluating the data, this average peak voltage was estimated by scaling from the sugar crystal calibration data. Another source for this constant is to use the average power scattered by ice particles measured in the calibration tests at the University of Washington, as described in the next section. Using a sample in which the average particle mass was approximately the same as a 25 $\mu$  drop, the resulting average peak voltage is approximately three times smaller than the value initially used, and thus the calculated number densities of ice particles should be approximately three times larger. Even with this correction, the fraction of ice particles in the supercooled cloud was not over about 10 percent.

These tests showed clearly, however, that a large part of the ice observed may have been from sources other than the freezing of the supercooled drops. In particular, the lowest numbers of ice particles were found at the lowest temperatures. Second, the ice concentration did not fall to zero when the sprayers were stopped (with the wind tunnel still running). Third, the signal on the chart recorder had, in addition to a steady voltage presumably corresponding to the relatively numerous frozen drops, a number of individual spikes, corresponding to large ice crystals being detected. In some cases, snowflake-sized crystals of this kind could also be seen in the cloud, as viewed from the control room.

A possible explanation of these observations is that bulk liquid water was present around the sprayer, either due to aspiration from the supply lines when the sprayer was off, or impingement of drops on surfaces in the airflow. Large drops would separate from this water and freeze to form the observed large ice particles. At low temperatures, there would be less tendency for this water to remain liquid.

Finally, it is of interest that a few pulses were seen on the chart recorder before the sprayers were turned on for the first time. These presumably formed somewhere in the blower or cooler sections of the wind tunnel. These sections were located remotely, in a separate building from the test cell where the measurements were made.

## 6. CALIBRATION AT UNIVERSITY OF WASHINGTON

In April 1976, the ice particle counter was calibrated in the laboratory of Prof. L. Radke at the University of Washington. The objectives of this calibration were to verify that this instrument performed identically to the original UW ice particle counter on which it was based, and to obtain data relating the scattering cross section of typical ice particles to their physical dimensions and type.

The two ice particle counters were set up in the cold chamber there, with the two sampling tubes in line, attached by a short length of tubing. Air was drawn through these by a small blower. In operation, the cold chamber was brought down to temperature, then a cloud of water drops was sprayed into it. These drops were nucleated by exposing a length of copper rod that had been cooled in liquid nitrogen. The resulting crystals were then allowed to grow as described in Reference [1] (p. 192).

The pulses from the outputs of the two instruments were counted with digital counters, usually for a period of 60 seconds. This period was long enough so that errors caused by manually starting and stopping the counters were not significant. The output of the UW instrument came from a point in its circuit following a divide-by-two counter, and therefore this reading was multiplied by two before recording it. Simultaneously, a formvar replica was made of the crystals in the chamber. These replicas were used to determine the type and size distribution of the crystals being counted. An oscilloscope photograph was made of the output of the compressor-amplifier at the point where it was applied to the discriminators. This was a single sweep photograph usually of 0.2 seconds duration.

Both ice particle counters generate an output pulse when the detected power exceeds a certain threshold; the first step in the calibration was to adjust the ERT instrument so that this threshold agreed with the UW threshold. This was done by generating ice clouds containing many small ( $\sim 25\mu$ ) crystals and adjusting the voltage to the ERT instrument's phototube until there was consistent agreement between the two ice particle counters. This voltage was approximately 8.5v,

corresponding to  $G_{rel} = 3$ . This procedure was based on the fact that when the two thresholds are different, and the ice crystals supplied to the counters are near the threshold size, then there will be a number of particles that are larger than one threshold size but smaller than the other, causing a systematic difference in the number of particles detected.

Once the voltage to the phototube had been set in this way, it was found that the noise level, in relation to the threshold level, was the same for both instruments. It was not possible to directly compare the dc phototube currents, because of the ac coupled preamplifier of the UW ice particle counter.

Another way to have done this comparison would have been to use a pulsed light source such as a light-emitting diode that could be put in the scattering volume (with the laser off). The reason for not doing this is that light-emitting diodes emit over a relatively broad band, and thus the normal tolerance in the bandwidths of the interference filters would have caused large errors in the comparison.

Having set the thresholds, the relative counting rates of the two ice particle counters were compared as a function of the average maximum diameter of the particles collected on the formvar replicas. Figure 6-1 shows the agreement between them.

Figure 6-2 shows the histograms of pulse height and particle diameter for a typical cloud of ice particles, which consisted mostly of small plates and stars having smooth edges. As before, these measurements are compared to the theoretical predictions of Section 2 by associating the cutoff in the pulse height distribution with the cutoff in the particle size distribution. In this case, these are  $0.9 \times 10^{-10}$  w and  $75\mu$ , respectively.

Referring to the models of Section 2, Case 1, light transmitted through the face of the particle, predicts  $2.3 \times 10^{-12}$  w. To use models such as described in Case 2, with light transmitted parallel to the face, note that the fraction of the incident light scattered into the transmitting part of the mask depends on the thickness,  $d/6$ , which is  $12.5\mu$  in this case, while the depolarization is governed by the diameter. Thus, the predicted signal is  $1.05 \times 10^{-10} \times 12.5 \times \sin^2(75/288) = 0.87 \times 10^{-10}$ .

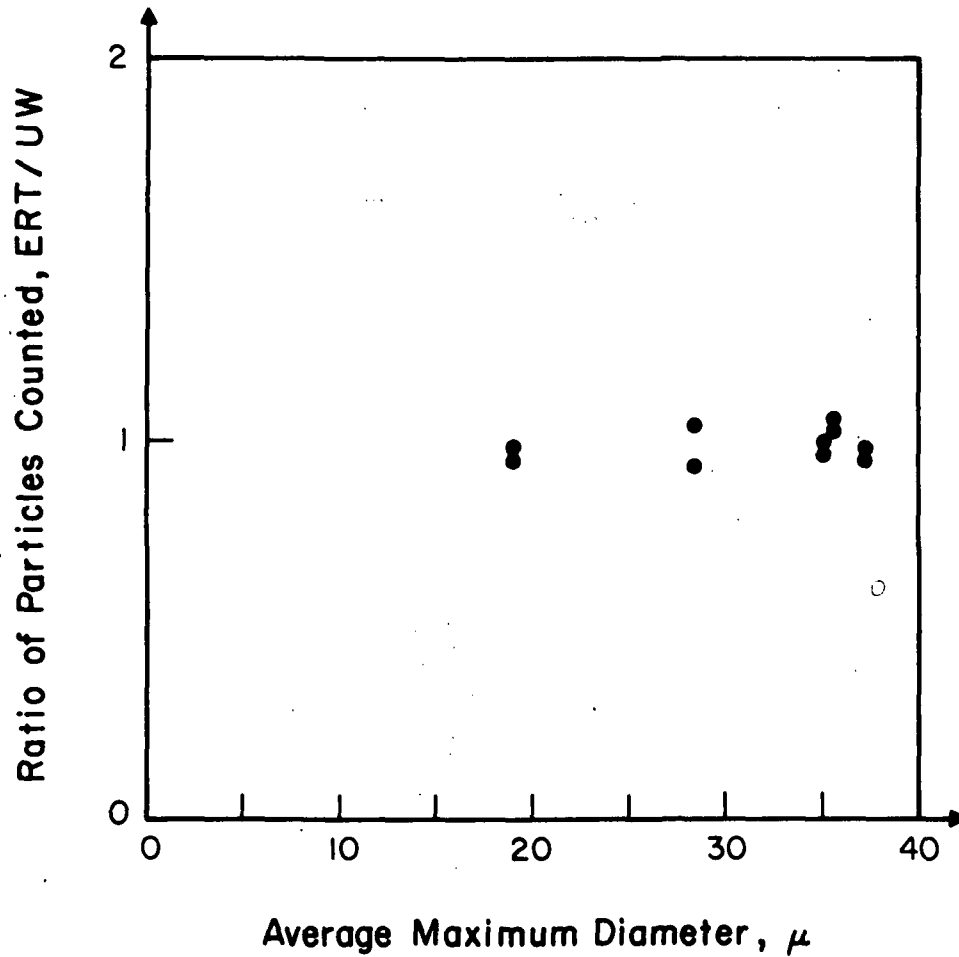


Figure 6-1 Relative Counting Rates of the Two Ice Particle Counters as a Function of the Average Maximum Diameter of Particles Being Counted  
The pairs of points are the results for counting immediately before and after the replica was taken, from which the particle size distribution was measured.

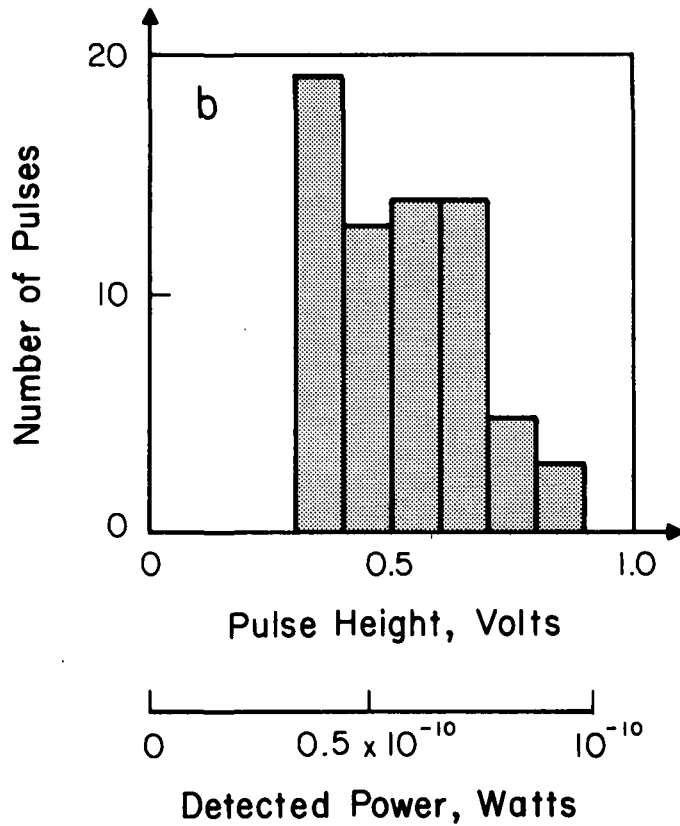
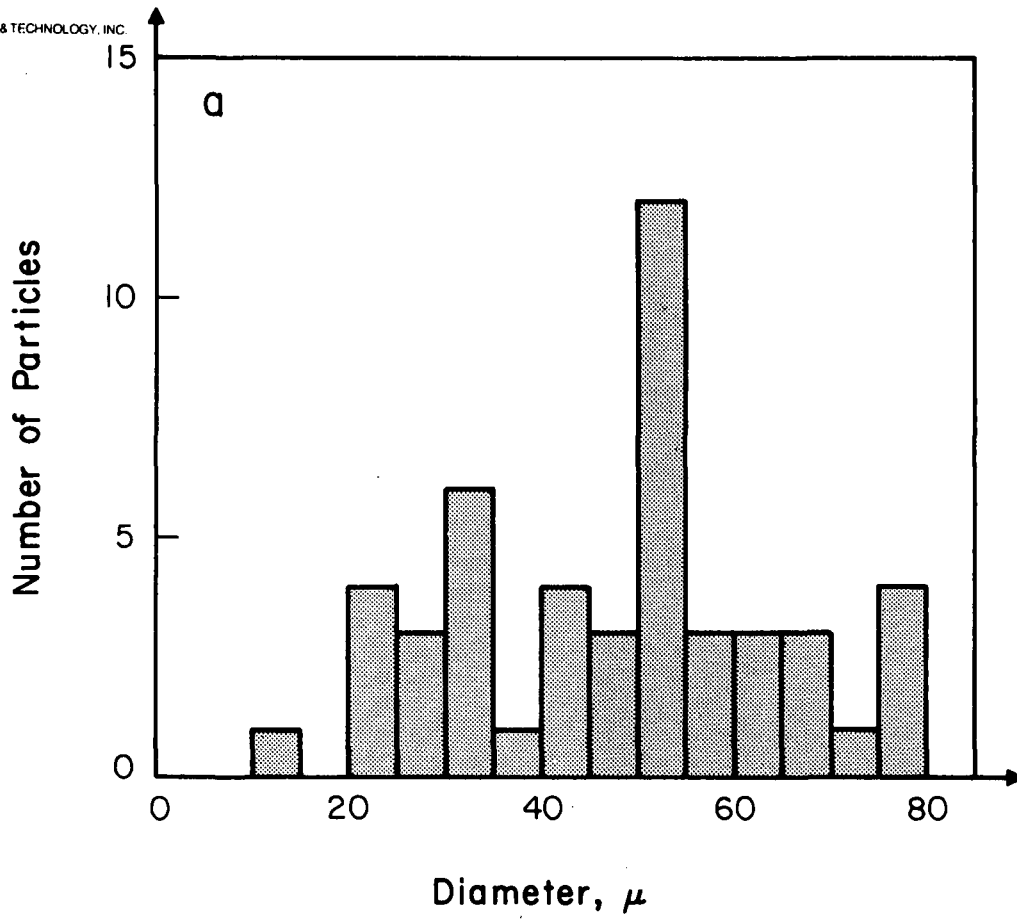


Figure 6-2b Pulse Height Distribution

This model by itself is not unreasonable, and it agrees with the observed signal. Unfortunately, the same features of the particle's geometry that permit this model to operate also permit light to be depolarized by internal reflection, thus resulting in a much larger signal.

If an additional assumption is made, i.e., that the edges are not flat, but instead are strongly curved about an axis parallel to the edge, so that most of the scattered light is deviated out of the field of view of the phototube, then the observed pulse height could be explained in a model involving internal reflection. The replicas do not provide much evidence to compare to this assumption. The surfaces of the edge facets are not visible for crystals that are captured in the formvar in the usual way. For those few crystals that are captured on the edge, the cross section of the edge does appear to be curved - usually concave - but this may be due to shrinkage of the formvar film.

In another typical case, the particles were mostly granules with diameters up to  $30\mu$ . The pulse height cutoff was  $0.33 \times 10^{-10}$  w. The theoretical models which might apply here are Case 2 and Case 6, with the later signal reduced because the crystals are not elongated and therefore, as in the measurements of salt crystals described in Section 5, only a small part of the entrance face transmits light that is ultimately depolarized by internal reflection.

For these particle dimensions, Case 2 predicts  $0.35 \times 10^{-10}$  w, while Case 6 predicts  $1.3 \times 10^{-8}$  w. Thus, even if the internal reflection model has a loss of 100x due to the near unity ratio of length to diameter, the predicted scattering is still much larger than the observed value.

In summary, for measurements on real ice crystals, scattering models in which the light is depolarized by internal reflection predict much larger signals than are actually observed, unless some mechanism such as scattering through large angles is introduced to reduce the detected power. Models in which depolarization is by the birefringence of the ice predict the detected power more closely, but the geometry of these models is such that internal reflection would usually occur.

**Page Intentionally Left Blank**

## 7. CONCLUSIONS, SUMMARY, AND SUGGESTIONS FOR FUTURE RESEARCH

This report has described the design and construction of an ice particle counter, patterned after the one described in Reference [1], that is suitable for use on an aircraft such as the NASA CV-990, and that can provide information to complement that obtained by the GSFC Laser Nephelometer.

Calibration tests have shown that this ice particle counter responds to ice crystals in a substantially identical way as the original instrument, and thus the data of Reference [1], especially relating to the detection probability for a given size of particle, should apply to this instrument as well.

The calibration data have been compared to several simple models of possible light scattering mechanisms by ice crystals. In general, models in which light is scattered by diffraction and depolarized by the birefringence of the ice crystals predict scattering cross sections in reasonable agreement with those observed. What is unexplained, however, is why internal reflection, a far more efficient depolarizing means for small crystals, does not produce a much larger cross section than the experimental one. Thus, the theoretical understanding of light scattering by ice crystals is not yet adequate to permit full use to be made of the pulse height data available from this kind of instrument.

The following areas for future research and development seem especially worthwhile:

- 1) Reduction of the optical noise level. At present, the only means of suppressing radiation that has been scattered but not depolarized is the polarizers in the instrument. As a result, the current from the phototube in the absence of particles is about 600 times larger than the tube's intrinsic dark current at room temperature. This might be reduced by adding a lens before the phototube so that light from the scattering volume is approximately colimated, while the exit window of the laser, which is the main source of this background light, is imaged onto a stop.

- 2) Assuming that the above is possible, it may be feasible to detect both water drops and ice crystals in the same scattering volume. This would provide the ratio of ice particles to water drops without needing to use two separate instruments, with all the attendant problems of cross calibration. In doing this, the light presently blocked by the mask in the regions  $45^\circ$  from the open areas used now, would be sent to a separate phototube. It could be either all the light, as in the GSFC Laser Nephelometer, or it could be just the component polarized perpendicularly to the incident light. In that case, the signal would be smaller, but so would be the background light. In either case, a coincidence gate would be used to discriminate between ice and water according to the relative amplitudes of the two signals.
- 3) The problem of light scattering by ice crystals should be studied. The objective of such a study would be to find out how, and if, pulse height information can be used to find properties about the ice crystals in clouds such as their crystalline type, size, or mass distribution, instead of just their number density. Determining these factors might involve the use of a multichannel counter such as described above.

A straightforward way to study this question would be to pursue the method described by Blau et al., [6]. Another way utilizes the existing ice particle counter, with no optical or hardware changes. Since this counter uses dc coupled electronics, it can operate independently of the speed with which particles go through the scattering volume, except for a predictable threshold shift due to the statistical nature of the background noise.

Therefore, it would be set up in a cold chamber, as used in the calibration tests described in Section 6, but no blower would be used; the ice particles would pass through it in free fall, and would be replicated as they fell out of the sampling tube. The low speed signal that resulted may be processed easily to yield a joint estimate of the speed and peak amplitude. This is possible because, as noted in Section 4,

the pulse width is independent of the distance of closest approach between the particle and the beam center. From the crystal type, known from the replica as long as most of the crystals are single type for any particular replica, and the speed, found above, the size of the particle is known. Thus, for each size particle of a given type, the data on pulse height will eventually yield a histogram of pulse heights. Deconvolving the effect of the Gaussian beam profile from this, the final result is the statistical scattering law for each size of ice particle of a particular type, all obtained with no hardware changes and only relatively straightforward signal processing.

**Page Intentionally Left Blank**

## 8. REFERENCES

- [1] Turner, F.M. The Design, Construction, and Evaluation of an Automatic Airborne Device for Counting Ice Particles in Clouds, PhD dissertation, University of Washinton, 1975. Availability: University Microfilms, Ann Arbor, Michigan.
- [2] Turner, F. M., and L. F. Radke. The Design and Evaluation of an Optical Ice Particle Counter, Journal of Applied Meteorology, V12, p. 1309-1318, (1973).
- [3] Principles of Optics, Born, M. and E. Wolf, 3rd Edition, Pergamon, New York, 1965, Section 14.2.3, p. 673.
- [4] ibid, p. 398.
- [5] Handbook of Mathematical Functions, ed. Abramowitz, M., and I. Stegun, Dover, N.Y., 1965, p. 364.
- [6] Blau, H. H., et al. Scattering by Individual Transparent Spheres Applied Optics, V9, p. 2522, (1970).

APPENDIX A

ASSEMBLY AND DISASSEMBLY INSTRUCTIONS  
FOR THE ICE PARTICLE COUNTER

APPENDIX A  
ASSEMBLY AND DISASSEMBLY INSTRUCTIONS FOR THE  
ICE PARTICLE COUNTER

To disassemble the ice particle counter, these procedures should be followed.

- 1) Remove the front fairing from the inlet tube. If it is equipped with a heater winding, disconnect it.
- 2) Remove the sampling tube, from the front. Note the presence of an alignment pin at the front end.
- 3) Remove the end plates.
- 4) With the end plates removed, the internal connectors for the power and signal wiring are accessible. Disconnect these, and pull the wiring out through the ends. Note that, to do this, the wiring and connectors on the aircraft end of the wiring must be able to fit through the access holes in the mounting flanges.
- 5) Remove the mounting flanges and their 3/8-16 bolts. Each flange has two parts, and these are conveniently kept together by putting temporary nuts onto the bolts. Note that the forward attachment bolt at the laser end is shorter than the others. Always double check that it is reassembled in the correct hole.
- 6) Put the alignment screws into the forward bolt hole at each end. Run them in so that the tops are below the wall of the outer shell.
- 7) Remove the allen-head screws in each web from the channel in the rear of the outer shell.
- 8) Slide out the interior parts.

To remove the phototube, the following procedures should be followed.

- 1) Disassemble as above.
- 2) Loosen the bolts that join the two aluminum plates of the clamping assembly (see Figure 3-4).

- 3) Run an 8-32, 2-inch bolt into each of the remaining holes of the clamp ring assembly. Using these as handles, pull out the clamp ring. This exposes the backup ring.
- 4) Thread the 1/4-20 rods into the holes in the backup ring.
- 5) Back out the alignment screw so that the backup ring may be withdrawn.
- 6) Using the long allen wrench, take out the three 6-32 screws from the flange of the phototube assembly. The phototube may now be removed, thus permitting one to slide the extension sleeve and web off the main spar.

Note that in all of the above, the term phototube refers to the complete assembly, consisting of the tube in a housing with the dc-dc converter, shielding, etc. The tube itself is potted in place, and not separately accessible.

The interference filter is cemented into a holder that screws into the Series V threads of the phototube flange. A rubber gasket seals this and prevents it from loosening.

The mask is located in front of the filter, and held against it by an O-ring, which is pressed against by the polarizer. The polarizer is held in place by a Series V adapter which screws into the threads of the filter assembly.

For correct operation, the mark on the polarizer, which indicates the axis of polarization, must be located in the middle of one of the open zones of the mask, and both must line up with one of the screw holes in the phototube flange. The phototube must be installed so that the axis of polarization is vertical, i.e. parallel to the flat surface on the back of the webs.

A blackened disk of metal foil is located in the center of the polarizer, to block the unscattered laser beam.

To remove the laser, the following procedures should be followed.

- 1) Remove the screws holding the laser power supply to the main spar. Note that the spar is used as a heat sink, and before replacing the power supply, heat-sink compound should be applied to the mating surfaces.

- 2) Disconnect the photocell used to monitor the laser's power output.
- 3) Remove the clamp ring from the end of the spar.
- 4) Being very cautious not to damage the leads of the laser, slowly rotate it back and forth to loosen it from the O-ring. This is also the manner in which the laser is rotated when setting the polarization.
- 5) Slowly work the laser back; as soon as it is clear of the O-ring, it will slide out freely.
- 6) Be certain not to lose the spacer ring that goes between the laser tube and the split and threaded part of the spar end.

Attached to the front of the laser is the polarizer used to suppress the incoherent light from the plasma tube.

To set the orientation of this polarizer, the following procedures should be followed.

- 1) Clamp the laser on any convenient workbench, table, etc. so it will not rotate.
- 2) Set an external polarizer so the laser's beam is extinguished.
- 3) Put the laser polarizer in place and adjust it so that the full beam is transmitted, and the second polarizer again extinguishes that beam.

This polarizer must also be set perpendicular to the beam, so that any multiple reflection between the laser output unit and the polarizer stays close enough to the principal beam to be blocked by the absorber on the phototube polarizer. This is done by adjusting the four screws that hold the polarizer assembly to the front of the laser.

To reassemble the ice particle counter, reverse the above disassembly instructions. Pay particular attention to the laser leads, and to avoid damage to them, NEVER adjust the laser orientation except when the outer shell has been removed and the laser leads can be seen clearly.

To set the laser's polarization, connect a high impedance (1 meg or more) voltmeter to the phototube output with the other circuitry

disconnected from it. The phototube output is marked "A". Turn on the laser and apply low voltage dc (not over 15v, + to the center conductor) to the input of the dc-dc converter, which is marked "LV". Adjust this voltage so approximately 0.1v reading results, then rotate the laser to bring this as close as possible to 0.

Note that the extension sleeve can rotate on the spar. Therefore, to insure that the webs are correctly aligned, the screws that attach the phototube flange to the spar should not be tightened completely until the outer shell has been slid over the laser web and partly over the phototube web.

In the event that the outer shell becomes dented so that the webs cannot slide out, note that the spar and extension sleeve can slide through the webs. Remove the forward attachment bolts, and back out the rear ones far enough so that the main spar is free, but the webs are held fixed. Note that the webs fit very closely; for this particular instrument, the web on the phototube end will not slide over the outer end of the extension sleeve. To permit removal in this way, never attach heater bands or the like with adhesives or permanent fasteners. Use lacing or spring clips, and always keep the surface of the spar clean and smooth.

The sampling tube has thin walls and is also fit very closely. When not in use, keep it in a crush-proof container. When installed on an aircraft, and not in use, make sure it is kept adequately protected, or at least is clearly marked "NO HAND HOLD".

When putting the ice particle counter into operation, the last step should be to seal the gap between the inlet tube fairing and the outer shell, preferably with an easily removed sealant such as silicone rubber.